Direct observations of electron firehose fluctuations in the magnetic reconnection outflow

G. Cozzani[1,2], Yu. V. Khotyaintsev[2], D. B. Graham[2], M. André[2]

[1]Department of Physics, University of Helsinki, Helsinki, Finland
[2]Swedish Institute of Space Physics, Uppsala, Sweden

Key Points:

- Magnetic reconnection exhausts host regions of enhanced electron temperature anisotropy where the electron firehose instability can develop
- We analyze waves associated with regions where the electron firehose instability (EFI) threshold is exceeded
- We report direct in situ observations of the non-propagating electron firehose wave mode in the magnetic outflow region in the magnetotail

Corresponding author: G. Cozzani, giulia.cozzani@helsinki.fi

Corresponding author: Yu. V. Khotyaintsev, yuri@irfu.se

Abstract

Electron temperature anisotropy-driven instabilities such as the electron firehose instability (EFI) are especially significant in space collisionless plasmas, where collisions are so scarce that wave–particle interactions are the leading mechanisms in the isotropization of the distribution function and energy transfer. Observational statistical studies provided convincing evidence in favor of the EFI constraining the electron distribution function and limiting the electron temperature anisotropy. Magnetic reconnection is characterized by regions of enhanced temperature anisotropy that could drive instabilities – including the electron firehose instability – affecting the particle dynamics and the energy conversion. However, in situ observations of the fluctuations generated by the EFI are still lacking and the interplay between magnetic reconnection and EFI is still largely unknown. In this study, we use high-resolution in situ measurements by the Magnetospheric Multiscale (MMS) spacecraft to identify and investigate EFI fluctuations in the magnetic reconnection exhaust in the Earth's magnetotail. We find that the wave properties of the observed fluctuations largely agree with theoretical predictions of the non-propagating EF mode. These findings are further supported by comparison with the linear kinetic dispersion relation. Our results demonstrate that the magnetic reconnection outflow can be the seedbed of EFI and provide the first direct in situ observations of EFI-generated fluctuations.

Plain Language Summary

Space and astrophysical plasmas can be often treated as collisionless since they are sufficiently tenuous and warm and particle-particle collisions can be neglected. Because of the scarcity of particle-particle collisions, the local thermodynamics equilibrium is generally not established and collisionless processes play a key role in energy conversion and heating. As local thermodynamic equilibrium is not achieved, particle distribution functions can significantly depart from Maxwellian distribution functions, leading to the development of instabilities and the formation of waves. This study focus in particular on the electron firehose instability (EFI). It is established that the EFI constraints the electron distribution function but direct observations of the waves generated by EFI are still lacking. In this study, we use high-cadence spacecraft observations by the Magnetospheric MultiScale (MMS) spacecraft mission to identify and investigate waves generated by the EFI. We will focus on EFI observations during a magnetic reconnection event in the Earth's magnetotail. Magnetic reconnection is a fundamental process of energy conversion in collisionless plasmas and investigating the interplay between magnetic reconnection and instability such as the EFI is critical to fully understanding energy conversion in plasmas. Our results provide the first direct observations of waves generated by the EFI.

1 Introduction

Kinetic plasma instabilities driven by temperature anisotropies are known to play an essential role in collisionless plasma dynamics, scattering the particles and affecting particle heating and energy conversion between the electromagnetic fields and particles (e.g., Gary, 1993). Among these anisotropy-driven instabilities, the whistler anisotropy instability is excited by electron temperature anisotropy $T_{e,\parallel}/T_{e,\perp} < 1$ while the electron firehose instability (EFI) develops if $T_{e,\parallel}/T_{e,\perp} > 1$, where $T_{e,\parallel}$ and $T_{e,\perp}$ are the electron temperatures respectively parallel and perpendicular with respect to the background magnetic field. The EFI is believed to constrain the electron temperature anisotropy by inducing heating (cooling) in the perpendicular (parallel) direction with respect to the background magnetic field, thus leading to isotropization.

The EFI was described for the first time by Hollweg and Völk (1970) and W. Pilipp and Völk (1971). Then, Gary and Madland (1985) provided the parametric dependencies of the growth rate of the EF modes with the assumption of parallel propagation, i.e.

the wave vector **k** is directed parallel to the background magnetic field. One-dimensional Particle-In-Cell (PIC) simulations further investigated the properties of the parallel propagating EF mode (Messmer, P., 2002; Paesold, G. & Benz, A. O., 2003). However, studies using both analytical and numerical approaches demonstrated the presence of two distinct branches of the EFI (Gary & Nishimura, 2003; Li & Habbal, 2000; Camporeale & Burgess, 2008; Hellinger et al., 2014). These studies are based on linear theory and 2D PIC simulations. In particular, the linear kinetic dispersion theory predicts a propagating EF mode characterized by parallel propagation with respect to the background magnetic field, and a non-propagating EF mode predicted to develop for oblique wave-normal angles. In addition, the non-propagating EF mode is resonant with both ions and electrons, while the propagating EF mode is non-resonant with respect to electrons. The two EF modes have been labeled in different ways, depending on the characteristics that the different studies wanted to highlight. In this paper, we chose to refer to the two modes as non-propagating and propagating EF modes, similar to Camporeale and Burgess (2008). The former is called also oblique, resonant, and a-periodic mode in other studies; the latter is called parallel, non-resonant and periodic (Li & Habbal, 2000; Gary & Nishimura, 2003; López et al., 2022).

There is a consensus that the non-propagating (oblique, resonant) mode is characterized by a lower threshold and higher growth rate compared with the propagating (parallel, non-resonant) mode. Hence, in this study, we will focus exclusively on the non-propagating EF mode as it is expected to be more efficient than the propagating EF mode in constraining the electron temperature anisotropy. The properties of the EF modes will be presented in detail in Section 2, focusing in particular on the non-propagating EF mode.

In the past decades, the electron firehose instability has been investigated in particular in the context of solar wind plasmas (Verscharen et al., 2022, and references therein) since the EFI is invoked as one of the most significant possible isotropization mechanisms to explain the quasi-isotropic state of the solar wind electrons. Indeed, the electron distribution functions observed in the solar wind are much closer to isotropic distributions than expected by considering the Chew–Goldberger–Low (CGL) model (Chew et al., 1956) of a spherically expanding solar wind (Štverák et al., 2008). Hence, the development of temperature-anisotropy-driven instabilities could explain the discrepancy between the model and the observed quasi-isotropic electron distributions. Statistical observational studies have confirmed the scenario of the EFI being crucial for isotropization by showing that the temperature anisotropy is well constrained by the thresholds of temperature-anisotropy-driven instabilities, notably the whistler instability and the EFI (Štverák et al., 2008; Cattell et al., 2022). Recently, several studies were devoted to investigating the EFI by modeling the solar wind electron distribution with more accuracy (both focusing on the propagating EF mode only (Lazar et al., 2016; Shaaban et al., 2021) or including also the non-propagating mode (Shaaban et al., 2019)). This includes going beyond the bi-Maxwellian approximation and taking into account the complex structure of the solar wind electron distribution function – consisting of a thermal core, a suprathermal halo, and a field-aligned beam (Feldman et al., 1975; W. G. Pilipp et al., 1987). Other efforts have been devoted to the investigation of the EFI onset (Innocenti et al., 2019) and evolution (Camporeale & Burgess, 2008; Hellinger et al., 2014; Innocenti et al., 2019). These studies focus on the non-propagating EF mode, as it arises self-consistently in the simulations of expanding solar wind (Innocenti et al., 2019) and has the larger growth rate in all simulations, consistently with the predictions of the linear theory.

Despite the majority of the work having been devoted to the study of the EFI in the solar wind context, the EFI can arise in any space environment where the plasma is unstable to the instability. Statistical studies collected and analyzed electron distribution functions in different near-Earth plasmas. Gary et al. (2005) used Cluster data to investigate electron distributions in the magnetosheath, while Zhang et al. (2018) used THEMIS observations to study electron distributions at dipolarization fronts in the mag-

netotail. These studies show that the electron distribution functions are constrained by the EFI threshold, suggesting that the EFI plays an important role in shaping the distribution functions.

Magnetic reconnection is a fundamental plasma process that plays a key role in energy conversion, plasma heating, and particle energization in a variety of plasma environments (Biskamp, 2000). The magnetic reconnection process is characterized by regions of enhanced temperature anisotropy (Egedal et al., 2013) that can be the seedbed for temperature anisotropy-driven instabilities. Indeed, a 3D PIC simulation study recently reported the presence of EFI-generated fluctuations in the reconnection outflow region (Le et al., 2019). The particle scattering and wave-particle interaction processes induced by the development of the EFI could potentially affect the energy conversion and acceleration produced by the reconnection process. However, little is known about the interplay between magnetic reconnection and the EFI. More importantly, direct observations of the EFI-generated fluctuations are currently lacking.

In previous studies focusing on near-Earth plasmas the presence of the EFI has been detected somewhat *indirectly* by looking at the limited anisotropy of the electron distribution functions (Zhang et al., 2018; Gary et al., 2005). The effect of the EFI is commonly inferred from the fact that the electron distribution is bounded by the instability threshold. This approach is suitable for statistical studies but it does not allow for *direct* observations of the EF wave modes. In this study, we use high-resolution measurements of the Magnetospheric Multiscale mission (MMS) (Burch et al., 2016) to shed light on the EFI-generated waves in the Earth's magnetotail. We report MMS observations of the non-propagating EF mode in the magnetic reconnection outflow region observed by MMS during a current sheet flapping event in the magnetotail. We show that the observed electron temperature anisotropy is constrained by the EFI threshold and we present *direct* in situ observations of the EFI-generated fluctuations.

This paper is organized as follows: In Section 2, we review the properties of the EF modes based on linear dispersion theory, focusing in particular on the non-propagating EF mode. In Section 3, we introduce the MMS data products used in this study. In Section 4, we present an overview of the current sheet flapping event in the Earth's magnetotail that we used for the analysis and we discuss the selection criteria for the EF events. Then, we present the detailed analysis of the EF fluctuations observed during two of the selected EF events in Section 5. In Section 6 we compare the results of the in situ spacecraft observations with a numerical solver. Sections 8 and 9 present the discussion and the conclusions respectively.

2 Properties of Electron Firehose Modes

Linear kinetic dispersion theory predicts that a magnetized plasma can be unstable to the development of the EFI under the condition of presenting a sufficiently large electron temperature anisotropy and being sufficiently warm, i.e. with $\beta_{e,\parallel} > 2$ ($\beta_{e,\parallel} = 2\mu_0 n_e T_{e,\parallel}/B^2$, where μ_0 is the vacuum magnetic permeability, n_e is the electron number density and B is the ambient magnetic field). As mentioned in the Introduction, the linear theory predicts the presence of two distinct branches of the EFI. One is propagating (real frequency $\omega \neq 0$) and it is characterized by parallel propagation at small θ_{kB} (where θ_{kB} is the angle between the wave vector $\mathbf{k}$ and the background magnetic field); the other mode is non-propagating and predicted to develop for oblique wave-normal angles, θ_{kB}. For $\theta_{kB} > 30^\circ$ the mode was defined as oblique by several studies (Li & Habbal, 2000; Gary & Nishimura, 2003), while more recently Camporeale and Burgess (2008) considered a higher threshold of $\theta_{kB} \sim 50^\circ$ to discriminate between the parallel and oblique mode.

It is established by both analytical and numerical studies that the non-propagating (oblique, resonant) mode is characterized by a lower threshold and higher growth rate than the propagating (parallel, non-resonant) mode. Indeed, the growth rate γ of the non-propagating mode is expected to be $\Omega_{ci} < \gamma < \Omega_{ce}$, while $\gamma < \Omega_{ci}$ for the propagating mode (Gary & Nishimura, 2003) (here $\Omega_\alpha = e\mathrm{B}/\mathrm{m}_\alpha$ is the cyclotron frequency, e the elementary charge and m_α the mass, $\alpha = \mathrm{e}, \mathrm{i}$ indicates the electron and ion species). For this reason, in the following, we will focus on the non-propagating EF mode only.

The EF instability threshold is predicted by the linear dispersion theory. The threshold depends upon the electron temperature anisotropy $\mathrm{T}_{\mathrm{e},\parallel}/\mathrm{T}_{\mathrm{e},\perp}$ and the parallel electron beta $\beta_{\mathrm{e},||}$ and in the following we will use to formulation reported by Gary and Nishimura (2003), which reads

$$\frac{\mathrm{T}_{\mathrm{e}||}}{\mathrm{T}_{\mathrm{e}\perp}} = \frac{1}{1 - \mathrm{S}'_{\mathrm{e}}/\beta_{\mathrm{e},||}^{\alpha'_{\mathrm{e}}}}. \tag{1}$$

The two primed quantities are dimensionless fitting parameters with $1 \lesssim S'_e \lesssim 2$ and $\alpha'_e \lesssim 1$ which are defined for $2 \leq \beta_{e,||} \leq 50$. For an instability growth rate $\gamma/\Omega_{\mathrm{ce}} = 0.001$, $S'_e = 1.29$ and $\alpha'_e = 0.97$.

The non-propagating EF mode is resonant with both ions and electrons. To establish if a mode is resonant or non-resonant with a plasma species, one can evaluate the Landau resonance factor $\zeta_\alpha = \omega/\sqrt{2}|k_\parallel|v_{\mathrm{th},\alpha}$ and the cyclotron resonance factor $\zeta_\alpha^\pm = |\omega \pm \Omega_{\mathrm{c}\alpha}|/\sqrt{2}|k_\parallel|v_{\mathrm{th},\alpha}$. Here, $|k_\parallel|$ is the magnitude of the wave vector component parallel to the background magnetic field and $v_{\mathrm{th},\alpha}$ is the thermal speed. In particular, for resonant species, which strongly interact with the waves, the resonant velocity is expected to lay within a thermal speed of the distribution function peak, satisfying the condition $\zeta_\alpha, \zeta_\alpha^\pm \lesssim 1$. Instead, for non-resonant species $\zeta_\alpha, \zeta_\alpha^\pm \gg 1$ (Gary et al., 1984). For a non-propagating mode, the Landau resonant factor is $Re(\zeta_\alpha) = 0$.

Figure 1 shows the properties of the non-propagating EF mode for $\beta_{e,||} = 9$ and $\mathrm{T}_{\mathrm{e},\parallel}/\mathrm{T}_{\mathrm{e},\perp} = 2$. The value of $\beta_{e,||} = 9$ is representative of the magnetotail plasma sheet conditions. Figure 1 is obtained with the numerical solver Plasma Dispersion Relation Kinetics (PDRK, (Xie & Xiao, 2016)) which solves the kinetic linear dispersion relation for multi-species plasmas in the magnetized electromagnetic case. The model implemented in the solver assumes that the plasma density is homogeneous, as well as the background magnetic field. The properties are shown in the parameter space composed of the normalized wave vector $\mathrm{k}\rho_\mathrm{e}$ and the wave-normal angle θ_{kB} (ρ_e is the electron Larmor radius). Figure 1(a) shows that this choice of input parameters leads to positive growth with a maximum rate $\gamma_{max}/\Omega_{\mathrm{ce}} \sim 0.13$. A positive growth rate is found for $\mathrm{k}\rho_\mathrm{e} \lesssim 1$ and the wave vector at maximum $\gamma = \gamma_{max}$ is $\mathrm{k}\rho_\mathrm{e} = 0.66$. As discussed above, the non-propagating EF mode is associated with oblique wave-normal angle θ_{kB} and, for the chosen set of parameters, the wave-normal angle at the maximum growth rate is $\theta_{\mathrm{kB}} = 69°$ (see Fig.1(a)). Figure 1(b) confirms that the mode is non-propagating, as $\omega = 0$ in all points of the parameter space. To quantify the waves electrostatic and electromagnetic components we use the parameter $\mathcal{E}_{\mathrm{long}} = |\mathbf{E} \cdot \hat{\mathbf{k}}|^2/|\mathbf{E}|^2$ which is equal to 1 for a purely longitudinal electrostatic wave and equal to 0 for a transverse electromagnetic wave. Figure 1(c) shows that $\mathcal{E}_{\mathrm{long}} < 0.5$ in the region of significant positive growth rate meaning that the non-propagating EF mode is electromagnetic. In Figure 1(d) we show the ratio $\delta\mathrm{B}_\parallel/\delta\mathrm{B}$ where $\delta\mathrm{B}_\parallel$ is the fluctuating magnetic field parallel to the background magnetic field and $\delta\mathrm{B}$ is the total fluctuating magnetic field. The magnetic field fluctuations are predominantly transverse i.e. $|\delta\mathrm{B}_\perp|^2 \gg |\delta\mathrm{B}_\parallel|^2$. The $\delta\mathrm{E}_\parallel/\delta\mathrm{E}$ ratio (Fig. 1(e)) indicates that the electric field fluctuations are dominated by the component aligned with the background magnetic field. Then, Figure 1(f) shows the polarization of the electric field fluctuations. For non-propagating waves, the polarization can be defined as $P = i\frac{\delta\mathrm{E}_\mathrm{x}}{\delta\mathrm{E}_\mathrm{y}}$, where $\delta\mathrm{E}_\mathrm{x}$ and $\delta\mathrm{E}_\mathrm{y}$ are two components of the electric field fluctuations. In the solver,

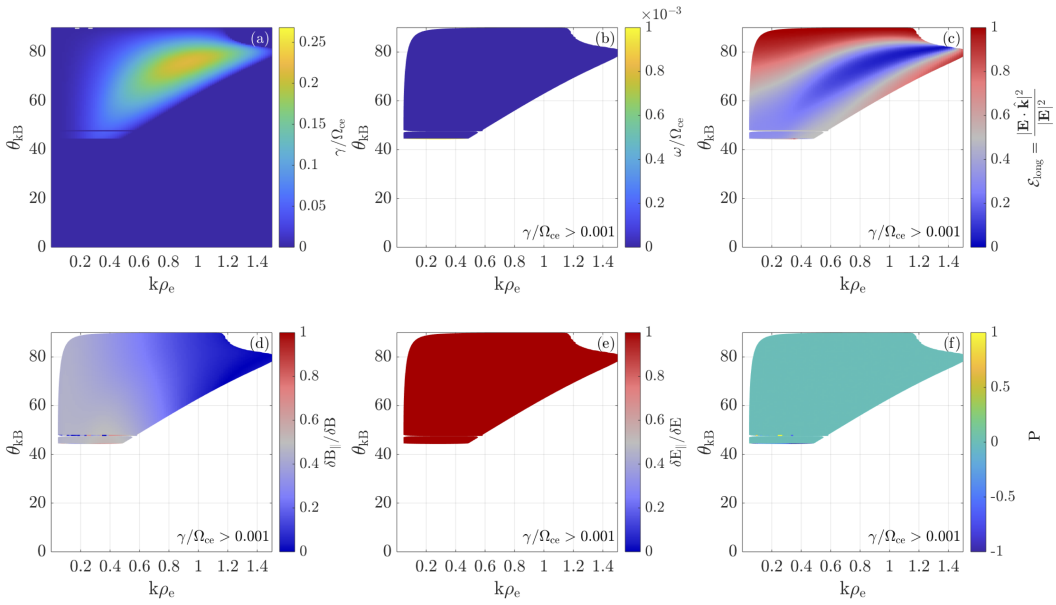

Figure 1. Properties of the non-propagating EF mode computed with the PDRK numerical solver. The input parameters used in the numerical solver are $T_{e,||} = 1000$ eV, $T_{e,\perp} = 500$ eV, the background magnetic field B = 3 nT and density $n_e = n_i = n = 0.2$ cm^{-3} while the isotropic ion temperature is $T_i = T_{i,||} = T_{i,\perp} = 4000$ eV. The panels show the parameters space $k\rho_e$–θ_{kB} versus (a) imaginary frequency γ/Ω_{ce} (b) real frequency ω/Ω_{ce} (c) $\mathcal{E}_{long} = |\mathbf{E}\cdot\hat{\mathbf{k}}|^2/|\mathbf{E}|^2$ (d) $\delta B_\parallel/\delta B$ (e) $\delta E_\parallel/\delta E$ (f) polarization $P = i\frac{\delta E_x}{\delta E_y}$. The quantities in panels (b)–(f) are shown for values of the growth rate exceeding the marginal stability condition, which is usually set at 10^{-3} (Camporeale & Burgess, 2008).

the background magnetic field is along the z direction while the wave vector $\mathbf{k} = (k_x, 0, k_z)$. As the polarization is 0 for all the values of $k\rho_e$ and θ_{kB} in Fig.1(f), the waves are expected to have a linear polarization.

In Section 5 we will consider several of the characteristics discussed above to identify fluctuations consistent with the non-propagating EF mode in MMS in situ observations. In particular, EFI-generated waves are expected to have zero real frequency and a wave vector $k\rho_e \lesssim 1$ directed obliquely with respect to the background magnetic field. The fluctuations are also expected to have a significant electromagnetic component (quantified via $\mathcal{E}_{long}$) and to be resonant with electrons.

3 Magnetospheric MultiScale (MMS) Data

We use data from the Magnetospheric MultiScale (MMS) spacecraft (Burch et al., 2016). In particular, we use the magnetic field **B** data from the fluxgate magnetometer (FGM) (Russell et al., 2016), electric field data **E** from the spin-plane double probes (SDP) (Lindqvist et al., 2016) and the axial double probe (ADP) (Ergun et al., 2016), and particle data from the fast plasma investigation (FPI) (Pollock et al., 2016). All data presented in this paper are high-resolution burst mode data. During the time interval selected for this study (15:24:00.0–15:58:00.0 UTC on 2017-07-06), the spacecraft were in a tetrahedral configuration with inter-spacecraft separation of $\sim$ 16 km. In the interval of interest, the average electron inertial length is 14 km, so the inter-spacecraft separa-

tion is comparable with the electron scales. Data from the MMS1 spacecraft are shown throughout the paper, as the observations are similar for the four spacecraft.

4 Event Overview and Data Selection

We consider a 34-minutes-long interval on 2017-07-06 when MMS was located at $[-24.1,\ 1.5,\ 4.4]$ R_E (in Geocentric Solar Magnetospheric GSM coordinate system) in the Earth's magnetotail. During this interval, MMS observes multiple crossings of the magnetotail current sheet, identified by the frequent B_x reversals (see Fig.2(a)). The plasma density (see Fig.2(c)) shows variations that are associated with the magnetic field. Higher values of the magnetic field (e.g. $|B| \sim 20$ nT at 15:40:02.7) correspond to lower densities ($n \sim 0.1$ cm^{-3}), indicating that MMS is sampling the lobe region, while lower values of magnetic field (e.g. $|B| \sim 1.5$ nT at 15:40:50.0) are associated with higher densities in the plasma sheet ($n \sim 0.26$ cm^{-3}). These observations indicate that the current sheet is flapping (e.g. Richard et al., 2021; Gao et al., 2018). During this interval, MMS often observes fast plasma flows. As shown in Fig.2(b), the x component of the ion velocity reaches values of $|V_{i,x}| \sim 1000$ km/s. The highest values are observed close to the neutral line $B_x \sim 0$ while the value of $V_{i,x}$ decreases toward zero when B_x increases which corresponds to MMS entering the lobe region. In the first part of the interval, $V_{i,x} < 0$ so the flow is directed tailward. At ∼15:46:41 MMS observes a flow reversal followed by strong Earthward flow with $V_{i,x} \sim 1000$ km/s. The observed flow characteristics suggest that MMS is sampling the magnetic reconnection outflow region, tailward outflow first and then Earthward flow. Similar conclusions were drawn in a study by Leonenko et al. (2021) focusing on the properties of super thin current sheets (sub-ion scale thickness) observed during the flapping event. We conclude that MMS observed a tailward retreating X-line in the magnetotail.

As the main goal of this study is the investigation of the EFI and the associated waves, we compute the instability threshold in order to identify the intervals in which the instability could develop. Figure 2(d) and 2(e) shows that there are several data points where $T_{e,\parallel}/T_{e,\perp} > 1$ and $\beta_{e,||} > 2$ at the same time, which is a necessary condition for the development of the EFI. Then, Figure2(f) shows the quantity $\mathcal{T}_{\rm EFI} = \frac{T_{e||}}{T_{e\perp}} - (1 - S'_e/\beta_{e,||}^{\alpha'_e})^{-1}$ which is obtained recasting Eq. 1. If $\mathcal{T}_{\rm EFI} > 0$ the threshold for the firehose instability is exceeded and the generation of waves is expected. We find 24 intervals with $\mathcal{T}_{\rm EFI} > 0$. Two time points t_1 and t_2 for which $\mathcal{T}_{\rm EFI} > 0$ are considered to be part of the same interval if $t_2 - t_1 < \tau$ where $\tau = 0.3\ s$. This value of τ corresponds to sub-ion time scales. In particular, it corresponds to one-third of an ion time scale computed considering a typical ion bulk velocity of 500 km/s and a typical d_i of 500 km based on the density value $n \sim 0.2$ cm^{-3} (see Fig.2(b)–(c)). However, the number of intervals does not change for $\tau = 0.5\ s$.

Figure 3 shows the distribution of the data points of the interval shown in Fig.2 in the parameter space $\beta_{e\parallel}$—$T_{e\parallel}/T_{e\perp}$, together with the EFI thresholds corresponding to growth rates $\gamma/\Omega_{ce} = 0.001$ (dark red curve), 0.01 (orange curve), and 0.1 (yellow curve) (see (Gary & Nishimura, 2003) for the values of the parameters used in the curves for different γ values). Only a few data points exceed the $\gamma/\Omega_{ce} = 0.001$ and 0.01 threshold, while no points are found above $\gamma/\Omega_{ce} = 0.1$, suggesting that the EFI plays a key role in shaping the electron distribution function.

From all the intervals where the threshold is exceeded, we select the ones composed of at least two data points and for which $\beta_{e,||} < 30$. We exclude intervals with large $\beta_{e,||}$ because, as it can be inferred from Fig.3, even small fluctuations of $T_{e,\parallel}/T_{e,\perp}$ due to instrumental noise can yield to $\mathcal{T}_{\rm EFI} > 0$ when $\beta_{e,||}$ is large, even though $T_{e,\parallel}/T_{e,\perp} \sim 1$ so that the available free energy would not be enough for the instability to develop. In addition, we select the intervals where magnetic field fluctuations could be identified by visual inspection, allowing us to thoroughly perform the wave analysis. Using these

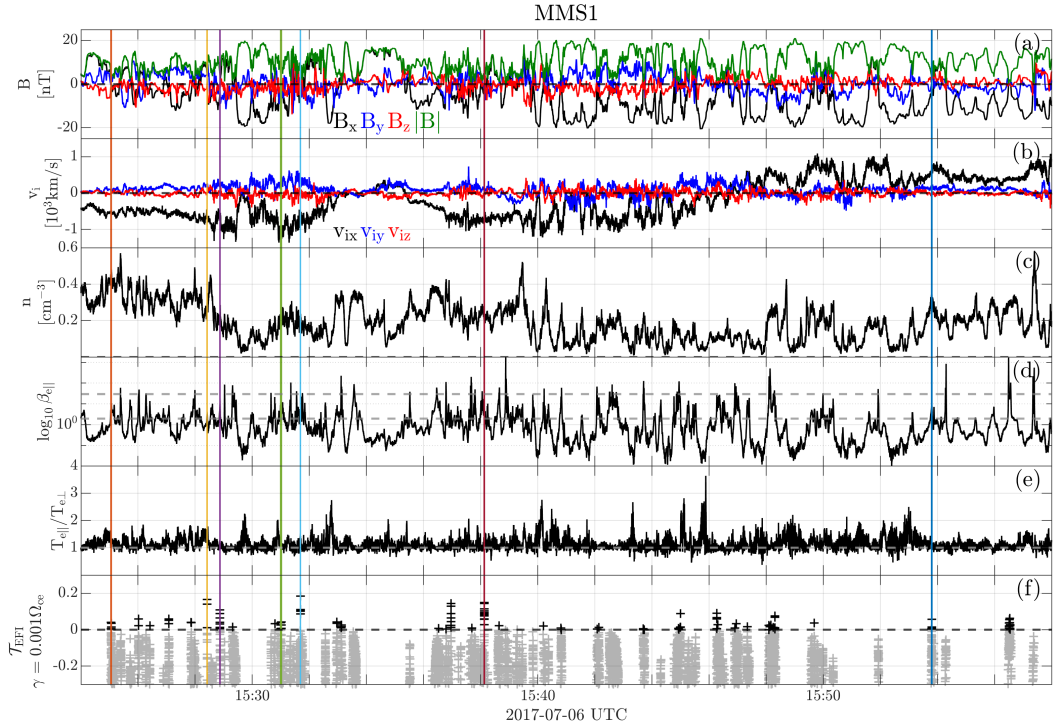

Figure 2. Overview of the current sheet flapping event in the Earth's magnetotail. (a) Magnetic field; (b) Ion velocity; (c) Ion number density; (d) $\log_{10} \beta_{e,\parallel}$, the grey horizontal dashed lines correspond to $\beta_{e,\parallel} = 2$ and $\beta_{e,\parallel} = 30$; (e) Electron temperature anisotropy $T_{e,\parallel}/T_{e,\perp}$. (f) Electron firehose instability threshold $\mathcal{T}_{EFI} = \frac{T_{e||}}{T_{e\perp}} - (1 - S'_e/\beta_{e,||}^{\alpha'_e})^{-1}$ for $\gamma = 0.001\Omega_{ce}$. Data points with $\mathcal{T}_{EFI} > 0$ (black crosses) are unstable to the EFI. The vertical colored lines indicate the intervals with $\mathcal{T}_{EFI} > 0$ that are selected based on the criteria discussed in Sec. 4 and that exhibit EF fluctuations.

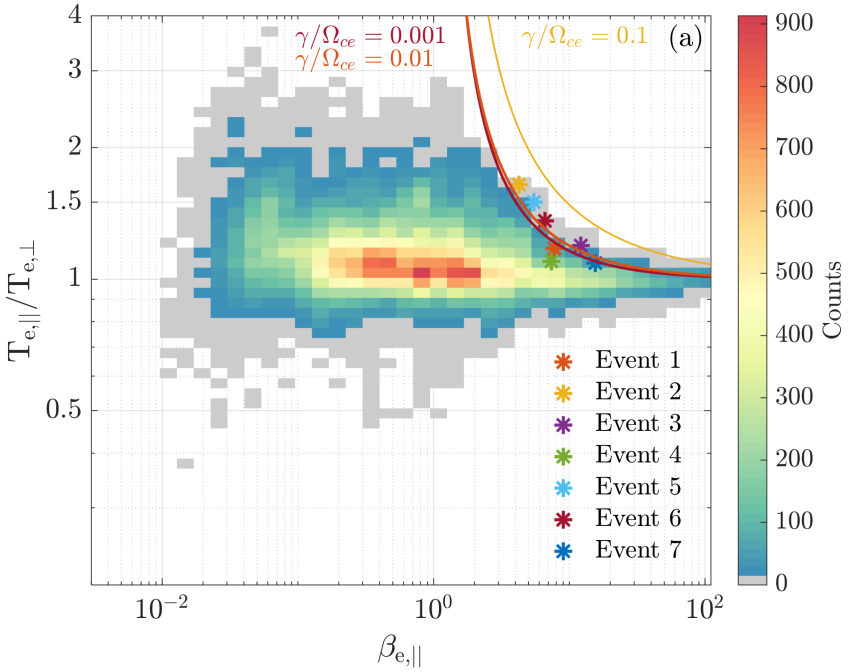

Figure 3. (a) Electron distribution in the parameter space $\beta_{e\|}$–$T_{e\perp}/T_{e\|}$. The counts are scaled with bin size. The curves corresponds to the EFI threshold (see Eq. 1) for growth rates γ/Ω_{ce}=0.001 (dark red curve), 0.01 (orange curve), and 0.1 (yellow curve). The colored stars mark the average value of $\beta_{e,\|}$ and $T_{e,\|}/T_{e,\perp}$ during the intervals of the selected events identified with the correspondingly color-coded vertical lines in Fig.2.

Table 1. Time intervals and characteristics of the events selected for the EF wave analysis. $\Delta t_{\mathcal{T}_{EFI}>0}$ is the time interval where the EFI threshold is exceeded.

#	$\Delta t_{\mathcal{T}_{EFI}>0}$ [UTC]	$\beta_{e,\parallel}$	$T_{e,\parallel}/T_{e,\perp}$	$T_{e,\parallel}$ [eV]	$T_{e,\perp}$ [eV]	T_i [eV]	|B| [nT]	n [cm^{-3}]
1	15:25:03.000–15:25:03.744	7.75	1.17	457	389	3259	3.3	0.47
2	15:28:25.070–15:28:25.134	4.24	1.64	1113	676	3840	5.8	0.32
3	15:28:52.010–15:28:52.284	12.17	1.19	1870	1567	4685	3.5	0.20
4	15:30:59.690–15:31:01.340	7.34	1.10	2678	2439	5178	5.5	0.20
5	15:31:41.150–15:31:41.300	5.46	1.50	2277	1516	5559	5.6	0.19
6	15:38:07.400–15:38:07.890	6.62	1.36	839	617	4844	3.3	0.22
7	15:53:47.700–15:53:48.430	15.48	1.12	668	596	4258	2.3	0.33

selection criteria, we retain seven intervals with $\mathcal{T}_{EFI} > 0$. They are marked with the vertical lines in Fig.2. The coloured stars in Fig.3 mark $\beta_{e,\parallel}$ and $T_{e,\parallel}/T_{e,\perp}$ averaged during the intervals identified with the correspondingly colour-coded vertical lines in Fig.2. The time intervals of the seven selected events are summarized in Table 1, together with the corresponding averaged plasma parameters.

In summary, we identify several intervals in which the EFI threshold is exceeded while MMS is sampling the outflow reconnection region in the Earth's magnetotail during a current sheet flapping event. After applying the selection criteria discussed above, we select seven events exhibiting wave activity at the time when the EFI threshold is exceeded. In the following, we will investigate the wave properties and establish whether the observed fluctuations are compatible with EFI-originated waves.

5 Wave Analysis

In this Section, we present the detailed wave analysis of two of the seven selected events (event #6 and #7), which we use to illustrate the typical wave properties. The other events are discussed later in section 7. Event #6 exhibits very clear wave activity and a significant electron temperature anisotropy peaking at $T_{e,\parallel}/T_{e,\perp} \sim 1.48$. However, the analyzed waves are not co-located with the interval where the EFI threshold is exceeded. So, we show also the detailed analysis of another event, event #7, during which we identify two intervals of wave activity. One is co-located with the interval with $\mathcal{T}_{EFI} > 0$ and the other, similarly to event #6, is observed immediately after the interval where the EFI threshold is exceeded. Also, event #6 is characterized by $V_{i,x} < 0$, meaning that MMS is observing the tailward reconnection outflow, while event #7 is observed in the Earthward outflow region. Hence, choosing these two events allows us to show the properties of the observed waves both in Earthward and tailward outflow regions. We aim to compare the observed wave characteristics to the theoretical expectations for EFI-generated fluctuations. As previously discussed, we focus on the non-propagating EF mode (oblique, resonant mode) as it is predicted to have a lower instability threshold and a larger growth rate with respect to the propagating (parallel, non-resonant) mode.

5.1 Event #6

An overview of event #6 is shown in Fig. 4. Figure 4(e) shows that during the interval $\Delta t_{\mathcal{T}_{EFI}>0}$=15:38:07.400–15:38:07.890, highlighted with the red-shaded area, the

temperature anisotropy $T_{e,\parallel}/T_{e,\perp}$ exceeds the EFI threshold (red line, see Eq. 1) and it reaches a maximum value of 1.5. In addition, $\beta_{e,\parallel}$ has moderate values ($\beta_{e,\parallel} \sim 7$ is the average $\beta_{e,\parallel}$ in the interval where the instability threshold is reached, see Fig.4(d)). The magnetic field is shown in Fig.4(a) and the relatively low magnitude of $|B| \sim 6$ nT suggests that MMS is sampling the plasma sheet. MMS also observed a strong electron (and ion, not shown) flow mainly directed along the x GSM direction with $|v_{e,x}| \sim 1500$ km/s suggesting that MMS is sampling the reconnection outflow region (see Fig.4(c)).

Figures 4(f) and (g) show the wavelet spectrograms of the electric and magnetic field power. Both electric and magnetic field power increase in the yellow-shaded interval. The fluctuations are rather broadband but they exhibit a peak at a few Hz, close to the lower hybrid frequency $f_{LH} = \sqrt{f_{ci} f_{ce}}$ (f_{ci} and f_{ce} are respectively the ion and electron cyclotron frequency). As a first step, we isolate the high-frequency fluctuations from the lower-frequency variations of the magnetic field. We define the filtering frequency f_{filt} by requiring that the magnetic field signal filtered in the frequency range $f < f_{filt}$ exhibits all the main magnetic structures of the unfiltered signal. In this case we choose $f_{filt} = 2.6$ Hz (see Fig.4(a)). The magnetic field exhibits low frequency variations ($f < f_{filt}$, Fig.4(a)) and, interestingly, higher frequency fluctuations ($f > f_{filt}$ showing wave activity Fig.4(b)). The interval with enhanced wave activity Δt=15:38:08.0–15:38:11.0 is highlighted by the yellow-shaded area. The magnetic field fluctuations $\delta\mathbf{B}$ have similar amplitude in all three components, both in the GSM coordinate system (see Fig.5(b)) and in field-aligned coordinates (see Fig.4(b)).

To better characterize the observed waves, we compute the dispersion relation from the phase differences of δB_z between spacecraft pairs, applying the multi-spacecraft interferometry method (Graham et al., 2016, 2019) to the time interval Δt. Figure 4(h) shows that the normalized power $P(f,k)/P_{max}$ increases in the frequency range 2.6 Hz $< f <$ 3.8 Hz (black dashed lines) with a peak at $f = f_{obs} = 3.2$ Hz (black star). The wave number at the $P(f,k)/P_{max}$ peak is $k\rho_e \sim 0.4$ ($\rho_e \sim 26$ km is the electron gyroradius averaged over Δt) which corresponds to the wave phase speed in the spacecraft reference frame of $v_{ph} \sim 900$ km/s. Figures 4(i) and (j) show that the wave vector $\mathbf{k}$ is directed mainly along the x direction, i.e. aligned with the direction of the plasma flow. The average wave vector direction is $\hat{\mathbf{k}} = [-0.82,\ 0.43,\ -0.38]$ GSM.

In addition, we estimate the uncertainty of the wave vector $\Delta k\rho_e$. Even though the $P(k_x,k_z)/P_{max}$ and $P(k_y,k_z)/P_{max}$ distributions exhibit a clear peak (Fig.4(i)–(j)), they are characterized by a certain spread in the (k_x,k_z) and (k_y,k_z) parameter space respectively. To compute the observed wave vector uncertainty $\Delta k\rho_e$, we consider all the points for which the power $P(k_i,k_j)$ is above 10% of the maximum power P_{max} in Fig.4(i)–(j), where $i,j = x,y,z$. The area selected with this criterion is shown in brighter colors in Fig.4(i)–(j). For each wave vector component k_j, the minimum k_j for which the power $P(k_i,k_j)$ is larger than 10% of the maximum power P_{max} is $k_{j,min}(P = 0.1P_{max})$. Analogously, $k_{j,max}(P = 0.1P_{max})$ is the maximum value of k_j for which the power $P(k_i,k_j)$ is equal or larger than 10% of the maximum power P_{max}. In general, $k_{j,min}(P = 0.1P_{max})$ and $k_{j,max}(P = 0.1P_{max})$ are asymmetric with respect to k_j corresponding to the maximum power. A simple way to symmetrize the uncertainty with respect to k_j is to use the average between the two uncertainties $k_{j,min}(P = 0.1P_{max})$ and $k_{j,max}(P = 0.1P_{max})$ so that the uncertainty $\Delta k_j\rho_e$ of the wave vector j^{th} component is $\Delta k_j\rho_e = \frac{\rho_e}{2}[k_{j,max}(P = 0.1P_{max}) - k_{j,min}(P = 0.1P_{max})]$. We then compute the uncertainty of the wave vector magnitude $\Delta k\rho_e$. We obtain $\Delta k\rho_e \sim 0.17 \sim 0.41 k\rho_e$ which is quite significant but expected, taking into account the considerable variability of the observed quantities.

Figure 5 shows additional characteristics of the observed fluctuations that are crucial to establishing whether the observed waves are indeed associated with the EFI. As discussed in Section 2, the non-propagating EF mode is characterized by zero real frequency $f = \omega/2\pi = 0$, $k\rho_e \lesssim 1$, the wave vector is directed obliquely with respect to the background magnetic field, and it is an electromagnetic mode. In addition, theoret-

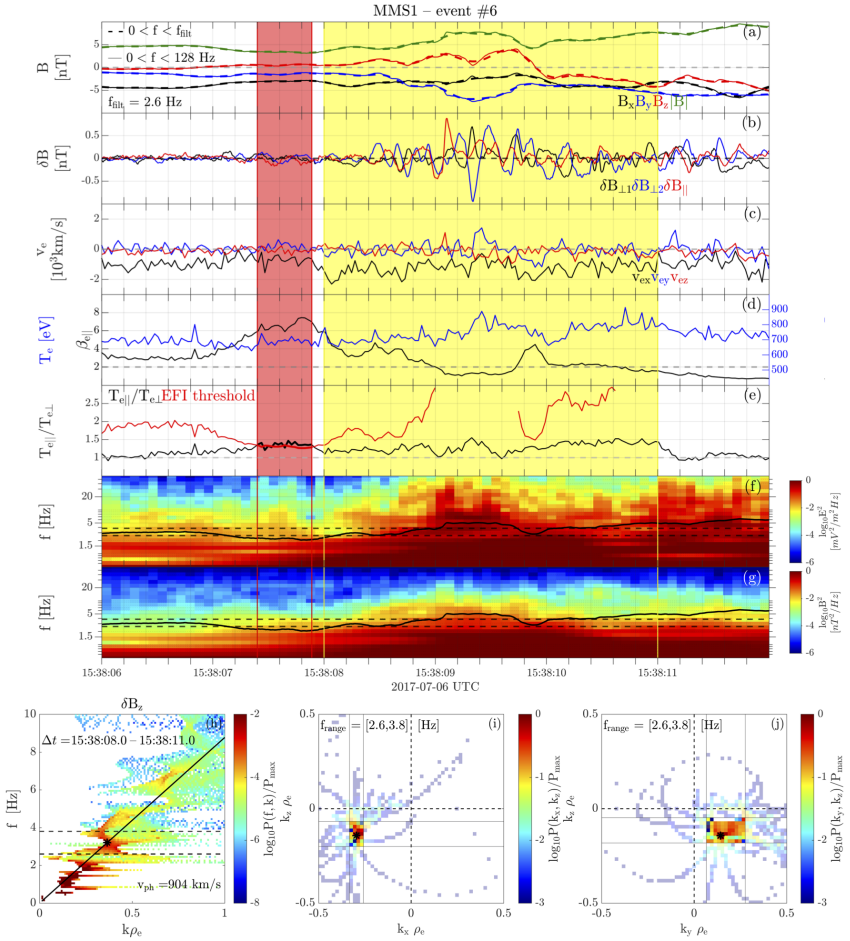

Figure 4. Top: (a) Magnetic field components and magnitude. The solid lines are the unfiltered magnetic field, with frequencies in the FGM frequency range $[0, 128]$ Hz, the dashed thick lines are the filtered signal with frequencies in the range $[0, f_{filt}]$ where $f_{filt} = 2.6$ Hz. (b) Magnetic field fluctuations ($f > 2.6$ Hz) in field-aligned coordinates (FAC). (c) Electron velocity. (d) $\beta_{e,\parallel}$ and electron temperature T_e. (e) Electron temperature anisotropy $T_{e,\parallel}/T_{e,\perp}$ and the EFI threshold based on Eq. 1. (f) Magnetic field wave power. (g) Electric field wave power. The black line is the lower hybrid frequency f_{LH} and the dashed black lines corresponding to $f = 2.6$ Hz and $f = 3.8$ Hz indicate the frequency range of the observed fluctuations. Bottom: Normalized power of magnetic field fluctuations δB_z versus (h) $k\rho_e$ and frequency f; (i) $k_x\rho_e$ and $k_z\rho_e$ (in the frequency range $\Delta f = [2.6, 3.8]$ Hz); (j) $k_y\rho_e$ and $k_z\rho_e$ (in the frequency range $\Delta f = [2.6, 3.8]$ Hz). The dashed lines in panel (h) correspond to $f = 2.6$ Hz and $f = 3.8$ Hz. The area with brighter color in panel (i) and (j) contains all the points with power $P(k_x, k_z)$ (and $P(k_y, k_z)$) larger than 10% of the maximum power P_{max}, i.e. $P(k_x, k_z) > 0.1P_{max}$ and $P(k_y, k_z) > 0.1P_{max}$.

ical expectations about the non-propagating EF mode include $\zeta_e^{\pm} \lesssim 1$, i.e. the mode is resonant with electrons.

Figure 5 shows that the characteristics of the observed fluctuations are compatible with the theoretical predictions listed above. Firstly, we establish that the observed mode is non-propagating in the plasma reference frame, i.e. the Doppler-shifted frequency is zero ($\mathrm{f_{obs}} - \mathrm{f_{DS}} = \mathrm{f_{obs}} - (\mathbf{v}_\mathrm{e} \cdot \mathbf{k})/2\pi = 0$, where $\mathrm{f_{DS}} = (\mathbf{v}_\mathrm{e} \cdot \mathbf{k})/2\pi$ is the Doppler shift frequency) or, equivalently, $\mathrm{f_{obs}} = \mathrm{f_{DS}}$. To do that, we compare the observed frequency of the fluctuations ($\mathrm{f_{obs}}$, red solid thick line in Fig.5(c)) to the Doppler shift frequency $\mathrm{f_{DS}}$ (black solid thick line in Fig.5(c)) in the time interval Δt where the waves are observed (yellow shaded interval in Fig.4). The Doppler shift frequency $\mathrm{f_{DS}}$ is significant as the wave vector $\mathbf{k}$ is quite aligned with the electron velocity $\mathbf{v}_e$. In particular, Fig.5(d) shows that $\theta_{\mathrm{kv_e}} < 60°$ during the considered time interval and the average $\langle\theta_{\mathrm{kv_e}}\rangle_{\Delta t} \sim 38°$, where $\theta_{\mathrm{kv_e}}$ is the angle between $\mathbf{k}$ and $\mathbf{v}_\mathrm{e}$. The time series of the Doppler shift frequency $\mathrm{f_{DS}}$ displays significant variations, which are due to the variations of the electron velocity $\mathbf{v}_\mathrm{e}$. To account for the variability of $\mathrm{f_{DS}}$, we compute $\sigma_{\mathrm{f_{DS}}}$ which includes the wave vector uncertainty $\Delta \mathrm{k}\rho_\mathrm{e}$ and the standard deviation of $\mathbf{v}_\mathrm{e}$ computed across the interval Δt. The quantity $\sigma_{\mathrm{f_{DS}}}$ corresponds to the uncertainty of $\mathrm{f_{DS}}$. The grey area in Fig.5(c) contains the points with $\mathrm{f_{DS}} - \sigma_{\mathrm{f_{DS}}} < \mathrm{f} < \mathrm{f_{DS}} + \sigma_{\mathrm{f_{DS}}}$ and defines the range of variability of $\mathrm{f_{DS}}$. Fig.5(c) also shows the time-averaged values across the interval ($\langle \mathrm{f_{DS}}\rangle_{\Delta \mathrm{t}} - \sigma_{\mathrm{f_{DS}}}$, $\langle \mathrm{f_{DS}}\rangle_{\Delta \mathrm{t}}$, $\langle \mathrm{f_{DS}}\rangle_{\Delta \mathrm{t}} + \sigma_{\mathrm{f_{DS}}}$) as black dashed lines. The observed frequency $\mathrm{f_{obs}}$ lies between $\langle \mathrm{f_{DS}}\rangle_{\Delta \mathrm{t}} - \sigma_{\mathrm{f_{DS}}}$ and $\langle \mathrm{f_{DS}}\rangle_{\Delta \mathrm{t}} + \sigma_{\mathrm{f_{DS}}}$ and for the majority of the time points $\mathrm{f_{obs}}$ lies in the variability range of $\mathrm{f_{DS}}$. We conclude that the observed Doppler-shifted frequency is close to zero and the observed waves are hence non-propagating fluctuations.

Figure 5(d) shows that the wave vector is oblique with respect to the background magnetic field. Fig.5(e) shows the spectrogram of $\mathcal{E}_{\mathrm{long}}$ which, while displaying significant variability, assumes relatively low values for the majority of the interval. The value of $\mathcal{E}_{\mathrm{long}}$ averaged both in time across Δt and in the frequency range $\Delta f = [2.6,\ 3.8]$ Hz is $\langle \mathcal{E}_{\mathrm{long}}\rangle_{\Delta t, \Delta f} \sim 0.54$. This means that the fluctuations are not electrostatic and they have a significant electromagnetic component. Also, $\langle \zeta_e^{\pm}\rangle_{\Delta t} \sim 1.7$ (not shown), indicating that electrons have a relatively strong resonance.

Hence, we observe non-propagating fluctuations characterized by a wave vector $\mathrm{k}\rho_\mathrm{e} \sim 0.4$ directed obliquely with respect to the background magnetic field, with significant electromagnetic component, and resonant electrons. All these characteristics are consistent with the theoretical expectations for EFI-generated fluctuations.

5.2 Event #7

As shown in Fig.4, during event #6 the interval where the EFI threshold is exceeded ($\Delta \mathrm{t}_{\mathcal{T}_{\mathrm{EFI}}>0}$ = 15:38:07.400–15:38:07.890) and the interval exhibiting the strong wave activity (Δt = 15:38:08.000–15:38:11.000) are not co-located, albeit the waves are observed immediately after the region with $\mathcal{T}_{\mathrm{EFI}} > 0$. In this Section, we present the detailed analysis of event #7 which exhibits wave activity both co-located with and, like event #6, immediately after the interval with $\mathcal{T}_{\mathrm{EFI}} > 0$. The observed fluctuations during event #7 are very similar to the ones reported in event #6 and are also consistent with EFI-generated waves.

Figure 6 is analogous to Fig.4 for event #6 and it shows that during event #7 the EFI threshold is exceeded in interval $\Delta \mathrm{t}_{\mathcal{T}_{\mathrm{EFI}}>0}$ =15:53:47.700–15:53:48.430 between the vertical red lines (see in particular Fig. 6(e)), where $\beta_{\mathrm{e},\parallel}$ increases to a maximum value of 28 (Fig. 6(d)) as MMS is located close to the neutral line. The magnetic field magnitude is $|\mathrm{B}| \sim 2$ nT (Fig. 6(a)) and MMS observes a strong electron flow, mainly along the outflow in the GSM x direction reaching $|\mathrm{v_{e,x}}| \sim 1200$ km/s (Fig.6(c)). Figure 6(b) shows the magnetic field fluctuations $\delta\mathbf{B}$ ($\mathrm{f_{filt}} = 2.5$ Hz) which have similar amplitude in all three components in both intervals of wave activity. Both magnetic and electric

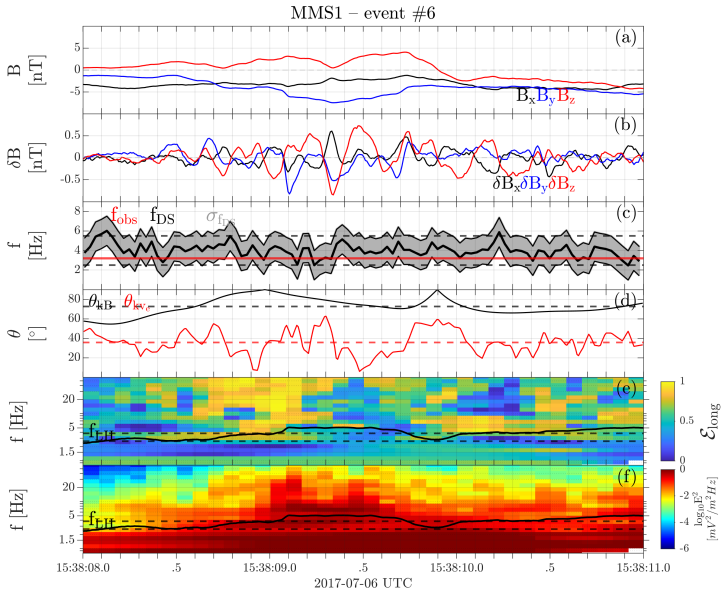

Figure 5. (a) Magnetic field; (b) Magnetic field fluctuations; (c) Observed frequency f_{obs} (red solid line), Doppler-shift frequency f_{DS} (solid black line) and associated variability range (grey shaded region) with value $\sigma_{f_{DS}}$. The central dashed black lines correspond to the time-averaged Doppler shift frequency $\langle f_{DS} \rangle$, the top and bottom dashed lines are $\langle f_{DS} \rangle + \sigma_{f_{DS}}$ and $\langle f_{DS} \rangle - \sigma_{f_{DS}}$. (d) Angle between the wave vector direction and background magnetic field direction θ_{kB} and angle between the wave vector direction and electron velocity direction θ_{kv_e}. (e) Spectrogram of $\mathcal{E}_{long}$. (f) Spectrogram of the electric field power. The black line is the lower hybrid frequency f_{LH} and the dashed black lines indicate the frequency range of the observed fluctuations ($\Delta f = [2.6, 3.8]$ Hz). The time interval shown in this figure corresponds to the yellow-shaded interval in Fig.4.

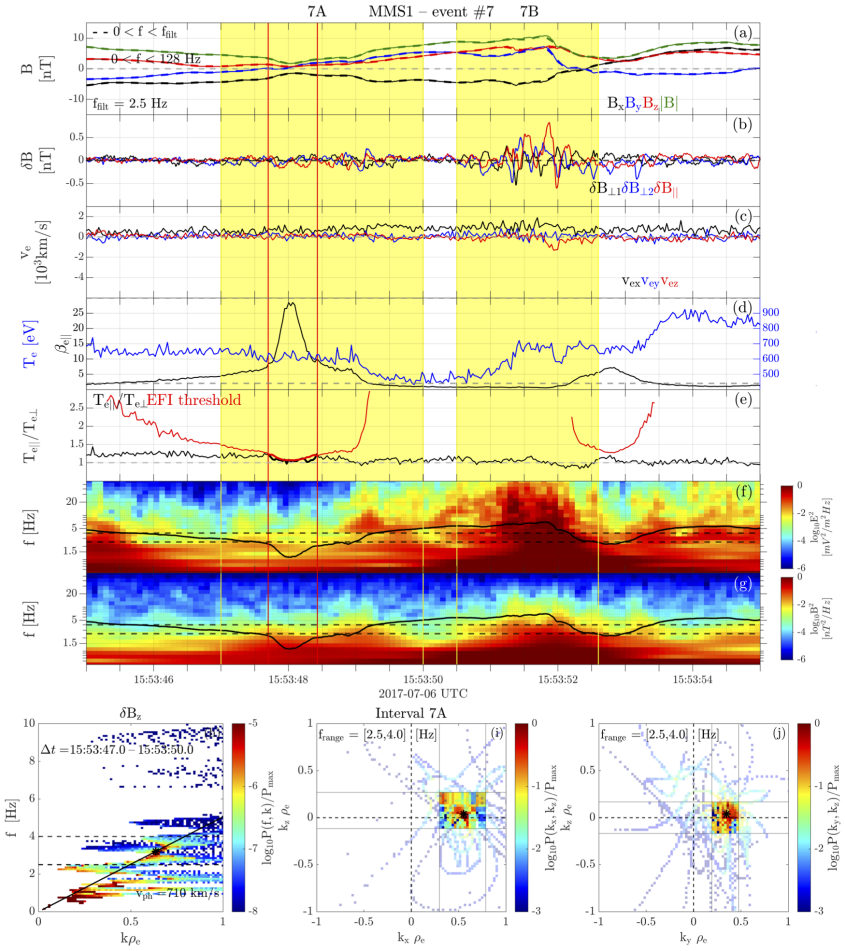

Figure 6. Same as Fig.4 for event #7. In this case, f_{filt} = 2.5 Hz. The bottom panels show the results of the multi-spacecraft interferometry method applied to interval 7A and The dashed lines in panel (h) correspond to f = 2.5 Hz and f = 4.0 Hz.

field power increase in the intervals with wave activity (Fig.6(f) and (g)). As mentioned above, we identify two intervals characterized by wave activity: interval 7A (Δt_A = 15:53:47.0–15:53:50.0), which encloses the interval with $\mathcal{T}_{EFI} > 0$ and interval 7B (Δt_B = 15:53:50.5–15:53:53.0). The fluctuations have larger amplitude in interval 7B, which is not co-located with the interval where the instability threshold is exceeded. In the following, we will focus in particular on the analysis of the fluctuations observed in interval Δt_A.

We use the multi-spacecraft interferometry method (Graham et al., 2016, 2019) to establish the characteristics of the fluctuations in Δt_A. The normalized power of the magnetic field fluctuations $P(f,k)/P_{max}$ increases in the frequency range $\Delta f = [2.5, 4.0]$ Hz (black dashed lines in Fig.6(h)) and peaks at $f = f_{obs} = 3.2$ Hz (black star). The wave number at the peak of δB_z normalized power $P(f,k)/P_{max}$ is $k\rho_e \sim 0.66$ ($\rho_e \sim 22$ km is the electron gyroradius averaged over interval 7A) which corresponds to phase speed in the spacecraft reference frame of $v_{ph} \sim 710$ km/s. Figure 6(i) and (j) shows that the wave vector **k** is directed mainly along x GSM and aligned with the direction of the outflow ($\hat{\mathbf{k}}$ = [0.78, 0.61, 0.03] GSM). Analogously to event #6, we estimate the uncertainty of the wave vector magnitude $\Delta k\rho_e$ and we obtain $\Delta k\rho_e \sim 0.22 \sim 0.33$ $k\rho_e$.

Similarly as Fig.5 for event #6, Figure 7 shows the property of the fluctuations in interval 7A to establish whether the observations are consistent with theoretical expectations for the EF fluctuations. Fig.7(a) indicates that the waves observed in Δt_A can be considered as non propagating, as f_{obs} lies between $\langle f_{DS}\rangle_{\Delta t} - \sigma_{f_{DS}}$ and $\langle f_{DS}\rangle_{\Delta t} + \sigma_{f_{DS}}$ and for the majority of the time points f_{obs} lies in the variability range (gray area of Fig.7(a)) of f_{DS}. Also in this case, the contribution of f_{DS} to the Doppler shifted frequency is significant as $\langle \theta_{kv_e}\rangle_{\Delta t} \sim 36°$ in interval 7A (see Fig.7(d)).

Other characteristics of the fluctuations in interval 7A include $\langle \mathcal{E}_{long}\rangle_{\Delta t,\Delta f} \sim 0.23$, indicating that they are electromagnetic (in this case $\Delta f = [2.5, 4.0]$ Hz). The spectrogram of $\mathcal{E}_{long}$ is shown in Fig.7(e) and despite exhibiting some variability, it never reaches values close to 1 in the considered Δf during interval 7A. Also, electrons are resonant since $\langle \zeta_e^{\pm}\rangle_{\Delta t} \sim 1.2$ (not shown). The angle between the wave vector and the background magnetic field θ_{kB} changes significantly in interval 7A, going from a minimum value of $\theta_{kB} \sim 30°$ to values close to 90° (Fig.7(d)), while the time-averaged value of the wave normal angle is $\langle \theta_{kB}\rangle_{\Delta t} \sim 69°$. The strong variation of θ_{kB} across Δt_A is due to the changing background magnetic field direction. In particular B_y goes from negative $B_y \sim -1$ nT to positive $B_y \sim 5$ nT in the considered interval. However, for the majority of the interval $\theta_{kB} > 30°$, so that the wave vector can be considered to be oblique with respect to the background magnetic field.

In summary, we observe non-propagating fluctuations with wave vector $k\rho_e \sim 0.66$ directed obliquely with respect to the background magnetic field. The fluctuations have a significant electromagnetic component and are resonant with electrons. We conclude that the observed fluctuations are generated by the EFI instability as they exhibit the characteristics associated with the non-propagating EF mode. As mentioned above, event #7 presents two intervals with wave activity. We have shown the detailed wave analysis of the fluctuations in interval 7A, which are co-located with the region where the EFI threshold is exceeded. The fluctuations with larger amplitude observed in interval 7B have similar characteristics (not shown) and we conclude that they are also EFI-generated waves. It is reasonable to expect that the development of the waves and the increase in the wave amplitude results in a decrease in the temperature anisotropy, which is reduced to a value close to isotropic.

6 Comparison between In Situ Observations and Model

To corroborate our conclusion that the observed fluctuations are EFI-generated, we compare the MMS observations with the results of the numerical solver PDRK (Xie & Xiao, 2016), which has been used to obtain Fig.1. The model implemented in the solver assumes that the plasma is homogeneous, as well as the background magnetic field. We consider a quasi-neutral plasma composed of electrons and protons. In the following, we will refer to the protons as ions, for consistency with MMS notation. We use a non-drifting bi-Maxwellian distribution function with $T_{e,||}/T_{e,\perp} > 1$ for electrons and a non-drifting Maxwellian distribution function for ions as input. The ion temperature is assumed to be isotropic $T_i = T_{i,||} = T_{i,\perp}$. This approximation is motivated by the fact that the non-propagating EF mode is not affected by the ion temperature anisotropy (López et al., 2022; Maneva et al., 2016). The PDRK solver input parameters are obtained by averaging the relevant observed quantities in the interval $\Delta t_{\mathcal{T}_{EFI}>0}$, where the EFI threshold is exceeded. The input parameters for the seven observed events are collected in Table 1. To avoid confusion, in this section the quantities that resulted from the analysis of in situ spacecraft observations are labeled with the subscript [obs].

Figure 8 shows the results of the PDRK solver with input parameters mimicking the in situ observations of event #6. A positive growth rate γ is obtained for several points in the parameter space $k\rho_e$–θ_{kB} with the maximum growth rate $\gamma_{max}/\Omega_{ce} \sim 0.025$ at $[k\rho_e, \theta_{kB}] = [0.54,\ 58°]$ (see Fig.8(a)). The unstable wave mode is characterized by zero

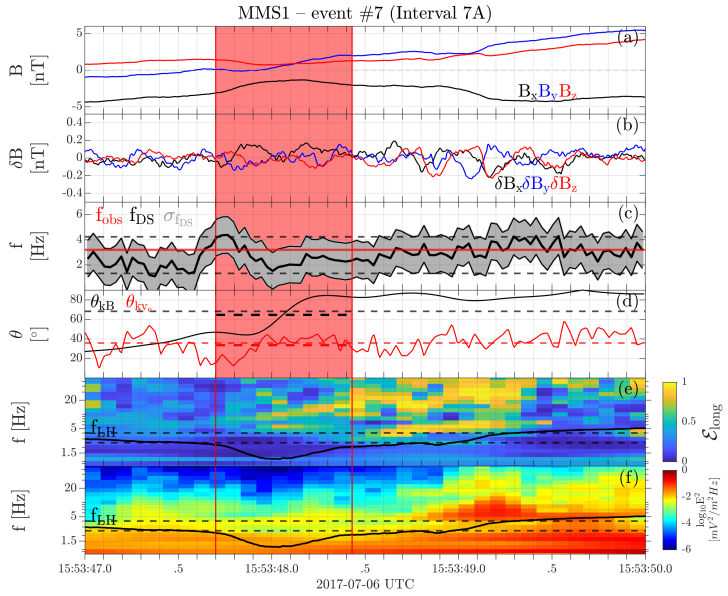

Figure 7. Same as Fig.5 for event #7 (interval 7A). In this case, the interval with $\mathcal{T}_{\mathrm{EFI}} > 0$ (red-shaded region) is co-located with the wave activity. Panel (c) shows θ_{kB} and $\theta_{\mathrm{kv_e}}$. The dashed lines correspond to the average value of θ_{kB} and $\theta_{\mathrm{kv_e}}$ and they extend over the time interval where they are computed.

real frequency (see Fig.8(b)). The values of θ_{kB} associated with highest wave growth range between 52° and 64° and indicate that the mode is oblique (see Fig.8(a)). The values of $\mathcal{E}_{\mathrm{long}}$, which are below 0.8 for the majority of the points in the area of the parameter space with positive growth rate, indicate that the mode is electromagnetic (see Fig.8(d)). We conclude that the unstable mode is the non-propagating EF mode, as expected considering the imposed input electron distribution function with $\mathrm{T_{e,||}/T_{e,\perp}} > 1$.

Figure 8 shows that the results of the numerical solver are consistent with in situ observations, providing further evidence that the observed fluctuations are associated with the EFI. The observed $[\theta_{\mathrm{kB}}]_{\mathrm{obs}} \sim 61°$ and $[\mathrm{k}\rho_{\mathrm{e}}]_{\mathrm{obs}} \sim 0.41$, corresponding to maximum magnetic field fluctuations normalized power $\mathrm{P(k,f)/P_{max}}$ in Fig.5(h), are marked with red stars in Fig.8. The red-shaded area corresponds to the points in the parameters space which lay within $[\Delta\mathrm{k}\rho_{\mathrm{e}}]_{\mathrm{obs}}$ and $[\Delta\theta_{\mathrm{kB}}]_{\mathrm{obs}}$, the uncertainties of $[\mathrm{k}\rho_{\mathrm{e}}]_{\mathrm{obs}}$ and $[\theta_{\mathrm{kB}}]_{\mathrm{obs}}$. The estimation of the wave vector uncertainty $[\Delta\mathrm{k}\rho_{\mathrm{e}}]_{\mathrm{obs}}$ is detailed in Sec.5. The uncertainty of the wave-normal angle $[\theta_{\mathrm{kB}}]_{\mathrm{obs}}$, $[\Delta\theta_{\mathrm{kB}}]_{\mathrm{obs}}$, is computed by considering $[\Delta\mathrm{k_j}\rho_{\mathrm{e}}]_{\mathrm{obs}}$ and the background magnetic field direction averaged in the interval $\Delta\mathrm{t}_{\mathcal{T}_{\mathrm{EFI}}>0}$. As expected considering the significant variability of the observed quantities, the uncertainties are significant, $[\Delta\mathrm{k}\rho_{\mathrm{e}}]_{\mathrm{obs}} \sim 0.17 \sim 0.41[\mathrm{k}\rho_{\mathrm{e}}]_{\mathrm{obs}}$ and $[\Delta\theta_{\mathrm{kB}}]_{\mathrm{obs}} \sim 10° \sim 0.16\ [\theta_{\mathrm{kB}}]_{\mathrm{obs}}$. Nonetheless, Fig.8 shows a good agreement between the numerical results and the in situ observations, as the observational points composing the red-shaded area significantly overlap with the EFI unstable region predicted by the numerical solver. The comparison between the output of the numerical solver and in situ MMS observations further confirms the fact that the observed waves are EF fluctuations.

Analogously to Fig.8 for event #6, Figure 9 shows a good agreement between the in situ observations and the numerical solver results for interval 7A of event #7. Figure 9(a) shows that a positive growth rate γ is obtained for several points in the parameter space $\mathrm{k}\rho_{\mathrm{e}}$–$\theta_{\mathrm{kB}}$. The growth rate peaks ($\gamma_{\mathrm{max}}/\Omega_{\mathrm{ce}} \sim 0.01$) at $[\mathrm{k}\rho_{\mathrm{e}}, \theta_{\mathrm{kB}}] = [0.56,\ 56°]$

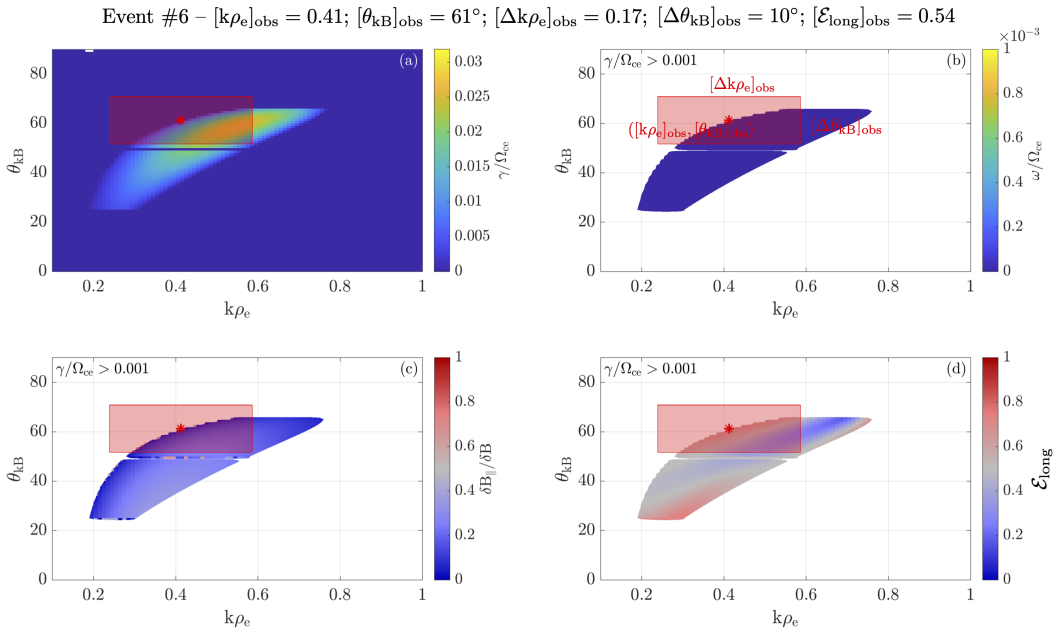

Figure 8. Observation–PDRK numerical solver comparison for event #6. The input parameters used in the numerical solver are $T_{e,||} = 839$ eV, $T_{e,\perp} = 617$ eV, the background magnetic field $B = 3.3$ nT and density $n_e = n_i = n = 0.22$ cm^{-3} while the isotropic ion temperature is $T_i = T_{i,||} = T_{i,\perp} = 4844$ eV (see Table 1). These values correspond to the average over the interval where the EFI threshold is exceeded ($\Delta t_{\mathcal{T}_{EFI}>0}$ =15:38:07.400–15:38:07.890). $k\rho_e$ and θ_{kB} versus (a) imaginary frequency γ/Ω_{ce} (b) real frequency ω/Ω_{ce} (c) $\delta B_\parallel/\delta B$ (d) $\mathcal{E}_{long}$. The quantities in panels (b)–(d) are shown for values of the growth rate exceeding the marginal stability condition, which is usually set at 10^{-3} (Camporeale & Burgess, 2008). The values listed above panel (a) and (b) correspond to the values observed in situ. In each subplot, the red star corresponds to the observed $k\rho_e$ and θ_{kB} at the peak of normalized power of the fluctuations (see Fig.4(h)–(j)). The red-shaded area represents the uncertainty of these measurements, $\Delta k\rho_e$ and $\Delta\theta_{kB}$.

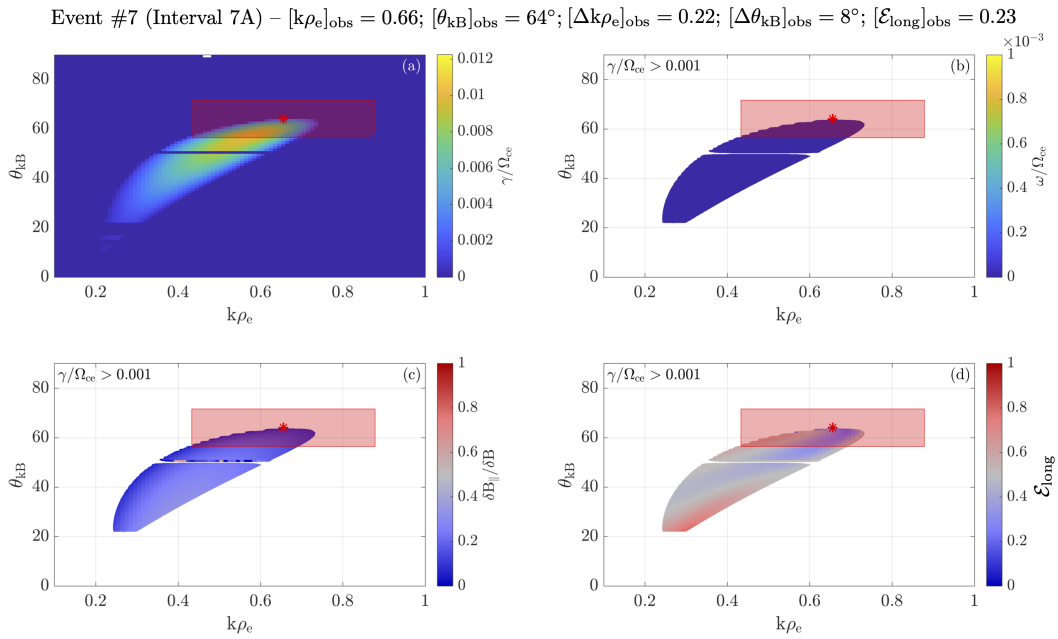

Figure 9. Observation–PDRK numerical solver comparison for event #7, analogous to Fig.8 for event #6. We use $T_{e,||}$ = 668 eV, $T_{e,\perp}$ = 596 eV, B = 2.3 nT, n_e = n_i = n = 0.33 cm^{-3} and T_i = $T_{i,||}$ = $T_{i,\perp}$ = 4258 eV, corresponding to the average over the interval where the EFI threshold is exceeded ($\Delta t_{\mathcal{T}_{EFI}>0}$ =15:53:47.700–15:53:48.430) as input parameters for the PRDK solver (see Table 1).

so the growing mode is rather oblique with respect to the background magnetic field. Fig.9(b) shows that all the points associated with $\gamma > 0$ have zero real frequency, so the mode is non-propagating. Also, $\mathcal{E}_{long} \lesssim 0.5$ for the majority of the points in the area of the parameter space with $\gamma > 0$, suggesting that the mode is electromagnetic (Fig.9(d)). Similar to what we concluded for event #6, these characteristics suggest that the unstable mode presented in Fig.9 is the non-propagating EF mode.

The wave analysis results of the observed fluctuations in interval 7A of event #7 are shown in Fig.9. In this case, the wave analysis of in situ observations gives $[k\rho_e]_{obs} \sim 0.66$ and $[\theta_{kB}]_{obs} \sim 64°$ and the associated uncertainties $[\Delta k\rho_e]_{obs} \sim 0.22 \sim 0.33\ [k\rho_e]_{obs}$ and $[\Delta\theta_{kB}]_{obs} \sim 8° \sim 0.13\ [\theta_{kB}]_{obs}$. During event #7 (interval 7A), as well as for event #6, we observe a good agreement between the in situ observations and the results of the numerical solver, reinforcing the conclusion that the observed fluctuations are indeed consistent with the non-propagating EF mode.

7 Other Events

As discussed in Section 4, during the interval shown in Fig.2 we have identified seven intervals fulfilling $\mathcal{T}_{EFI} > 0$ together with the selection criteria involving the number of consecutive data points with $\mathcal{T}_{EFI} > 0$, the value of $\beta_{e,||}$ and the presence of wave activity. For each of the events, we perform the detailed wave analysis presented in Sec. 5 and we compare the in situ observations with the numerical solver results, using the input parameters reported in Table 1. Each event is defined by the interval where the EFI threshold is exceeded ($\Delta t_{\mathcal{T}_{EFI}>0}$, see Table 1) and by the interval where the wave activity is observed (Δt, see Table 2). As already discussed in Sec.5, event #7 presents two intervals (7A and 7B) with enhanced wave activity.

For all the selected events, the observed fluctuations have characteristics consistent with the non-propagating EF mode. The results of the analysis of the seven events are summarized in Fig.10 and Table 2. In Figure 10, the abscissa shows the event number #. Fig.10(a) shows the observed frequency f_{obs} (black star) and the Doppler shift frequency $\langle f_{DS} \rangle_{\Delta t}$ (grey star) with the error bars corresponding to the variability $\sigma_{f_{DS}}$ for each of the selected events. For all the events, f_{obs} lies in the variability range of $\sigma_{f_{DS}}$ so that the Doppler shifted frequency is close to zero and the fluctuations can be considered as non-propagating. An exception is event #4 since f_{obs} lies outside (but still very close to) the variability range of f_{DS}. We still include event #4 in the list of EF events as the other characteristics of the observed waves are consistent with the EF mode. Also, it is worth clarifying that the so-called f_{DS} variability range, $\sigma_{f_{DS}}$, does not have to be interpreted as a rigorously defined error of f_{DS}, but rather a qualitative estimation of the uncertainty. The same quantities shown in Fig.10(a), this time normalized by the lower-hybrid frequency f_{LH}, are shown in Fig.10(b). In all the events, the observed frequency is comparable with the local f_{LH}. Fig.10(c)–(f) show other characteristics that we take into account for the wave analysis in Sec.5. In all the events, the wave characteristics are quite similar. Notably, $k\rho_e$ ranges between 0.30 and 0.74 (Fig.10(c)); θ_{kB} ranges between 32° and 81° indicating that the observed mode is oblique (Fig.10(d)); $\langle \mathcal{E}_{long} \rangle_{\Delta t, \Delta f}$ ranges between 0.23 and 0.57 meaning that the observed waves have a significant electromagnetic component (Fig.10(e)). The parameter $\langle \zeta_e^{\pm} \rangle_{\Delta t}$ has a minimum value of 0.9 for event #4 and a maximum of 2.4 for event #7 (Fig.10(f)). Another common feature of the fluctuations observed in all the events is that all three $\delta\mathbf{B}$ components have similar amplitude (see Fig.5(b) and Fig.7(b) for event #6 and #7). Also, during all the events the electron and ion velocity, notably in the GSM x direction, are large ($|v_{e,x}| \gtrsim 800$ km/s and $|V_{i,x}| \gtrsim 500$ km/s, see Fig.2), indicating that all the intervals with EF waves and where the EFI threshold is exceeded are located in the magnetic reconnection outflow region.

We then compare the in situ observations of each event with the results of the numerical solver PDRK, analogously to Sec.5 and 6 for event #6 and #7 (interval 7A). The PDRK solver is run with initial parameters such as background magnetic field, density, and temperatures, tailored to each event (see parameters in Table 1). For event #4, the temperature anisotropy has been artificially increased in the solver by 23% (from the value $T_{e,\parallel}/T_{e,\perp} = 1.10$ observed in situ to $T_{e,\parallel}/T_{e,\perp} = 1.35$) in order to obtain an unstable EF mode. The fact that it is needed to consider a higher $T_{e,\parallel}/T_{e,\perp}$ value to obtain wave growth is not surprising as it is expected for the anisotropy to decrease as the instability develops and the waves grow. Since waves are directly observed in situ, the electron temperature anisotropy at the time of the observations is likely lower than the $T_{e,\parallel}/T_{e,\perp}$ at the time of the instability onset. For each event, we find a good agreement between in situ observations and the model (not shown) suggesting that the waves observed in the selected events are fluctuations generated by the EFI developing in the reconnection outflow.

8 Discussion

In this study, we investigate a current sheet flapping event in the Earth's magnetotail associated with strong flows in the x GSM direction indicative of ongoing magnetic reconnection. The flow is directed tailward during the first part of the interval and Earthward at the end of the interval, indicating that MMS observed a magnetic reconnection X-line retreating tailward. Magnetic reconnection regions such as the outflow can be characterized by strong temperature anisotropy so that temperature anisotropy-driven instabilities, such as the EFI, can develop at those locations.

Even though the EFI has been invoked to explain the constrained electron temperature anisotropy in a variety of plasma environments, direct observations of the EFI-generated waves were lacking. In this study, we report in situ MMS observations of EF

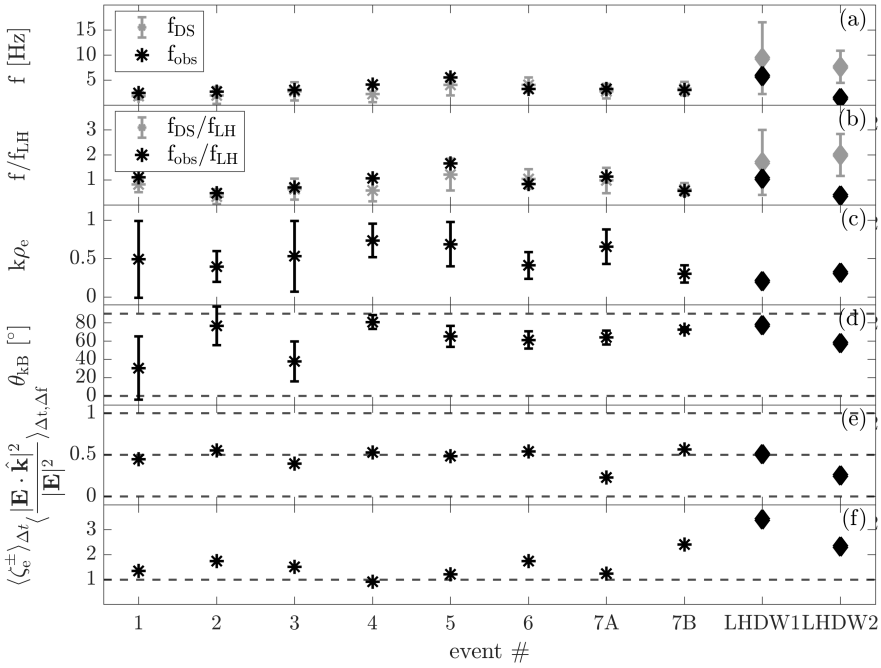

Figure 10. Fluctuations characteristics for the EF events (star markers) and two lower hybrid drift waves (LHDW) events observed in the magnetotail (diamond markers). Event LHDW1 and LHDW2 are reported respectively in (Chen et al., 2020) and (Cozzani et al., 2021). (a) Observed frequency f_{obs} and Doppler shift frequency averaged in the time interval of the fluctuations $\langle f_{DS} \rangle_{\Delta t}$ with the associated uncertainty $\sigma_{f_{DS}}$. (b) Same as (a) but frequencies are normalized to f_{LH}. (c) Wave vector magnitude $k\rho_e$. (d) θ_{kB}. (e) $\langle \mathcal{E}_{long} \rangle_{\Delta t, \Delta f}$. (f) $\langle \zeta_e^{\pm} \rangle_{\Delta t}$.

Table 2. Characteristics of the fluctuations of the EF events. Δt is the interval where the EF fluctuations are observed.

#	Δt [UTC]	f_{obs} [Hz]	$\langle f_{DS} \rangle_{\Delta t}$ [Hz]	$\sigma_{f_{DS}}$ [Hz]	$k\rho_e$	θ_{kB} [°]	$\langle \mathcal{E}_{long} \rangle_{\Delta t, \Delta f}$	$\langle \zeta_e^{\pm} \rangle_{\Delta t}$
1	15:25:03.0 – 15:25:04.6	2.4	1.8	0.7	0.49	32	0.45	1.3
2	15:28:24.6 – 15:28:27.2	2.7	1.9	1.7	0.40	77	0.55	1.7
3	15:28:51.4 – 15:28:53.8	3.0	2.7	1.8	0.53	38	0.39	1.5
4	15:30:58.5 – 15:31:01.5	4.1	2.2	1.7	0.74	81	0.53	0.9
5	15:31:41.9 – 15:31:42.7	5.5	4.0	2.1	0.69	65	0.48	1.2
6	15:38:08.0 – 15:38:11.0	3.2	4.0	1.5	0.41	61	0.54	1.7
7A	15:53:47.0 – 15:53:50.0	3.2	2.8	1.4	0.66	64	0.23	1.2
7B	15:53:50.5 – 15:53:53.0	3.0	3.3	1.3	0.30	73	0.57	2.4

waves in the reconnection outflow region. There are two distinct EF modes but, as specified above, we focus exclusively on the non-propagating EF mode since it has a larger growth rate and a lower instability threshold with respect to the propagating EF mode. While being located in the reconnection outflow, MMS observes several time intervals during which the EFI threshold is exceeded ($\mathcal{T}_{EFI} > 0$). Taking into account the selection criteria discussed in Sec. 4, we finally select seven events that are characterized by both $\mathcal{T}_{EFI} > 0$ and wave activity. We presented a detailed wave analysis of two of those events, showing that the observed wave characteristics are in agreement with the properties of the non-propagating EF mode.

Even though the non-propagating EF mode has distinct characteristics, it shares a few properties with the electromagnetic part of the lower hybrid mode. Lower hybrid drift waves (LHDW) are commonly observed in plasma regions characterized by strong spatial gradients in various quantities such as the density or the magnetic field. For example, the characteristics of the LHDW have been thoroughly investigated at the Earth's magnetopause (e.g., Graham et al., 2019). In the context of a current sheet, LHDW can be triggered by the lower hybrid drift wave instability (LHDI) and while an electrostatic, short wavelength ($k\rho_e \sim 1$) mode will be localized at the edges of the current sheet, an electromagnetic, longer wavelength ($k\sqrt{\rho_e \rho_i} \sim 1$) mode can be present at the center (Yoon et al., 2002; Daughton, 2003). The electrostatic mode is characterized by a larger growth rate but it stays confined at the edges of the current sheet, while the electromagnetic mode develops at later times and is present at the current sheet center (Daughton, 2003). The electromagnetic LHD mode is characterized by oblique propagation with respect to the background magnetic field and by frequency of the order of the lower hybrid frequency f_{LH}. So, both the electromagnetic LHD mode and the non-propagating EF mode are electromagnetic and characterized by large wave-normal angles. Despite these similarities, the two modes are of course distinct. Firstly, the EF mode is non-propagating so it has

zero real frequency, while LHDW have a frequency of the order of f_{LH}. Also, EFI-generated waves are expected to have a quite low $\delta B_{||}/\delta B$, while for obliquely propagating LHDW $\delta B_{||}$ is the largest component of the fluctuating magnetic field.

To further corroborate our results, we make sure that the fluctuations that we have identified as the EF waves are not the electromagnetic lower hybrid mode, which has been reported in several studies investigating magnetic reconnection in the Earth's magnetotail and at the magnetopause (Chen et al., 2020; Cozzani et al., 2021; Wang et al., 2022; Yoo et al., 2020). This further check is motivated by the fact that the observations are complex and characterized by significant uncertainties. The direct comparison with the LHD mode – which shares characteristics with the EF waves – will demonstrate that we are not mislabeling the observed waves and provide further robustness to our results. Thus, we will consider two LHDW events corresponding to reconnection electron diffusion region (EDR) crossings in the magnetotail reported by Cozzani et al. (2021) (on 2017-08-10 at 12:18:33.0) and Chen et al. (2020) (on 2017-07-03 at 05:27:07.5). As for the seven events discussed in previous sections, we computed the EFI threshold and we performed the wave analysis. The results are summarized in Fig. 10 (diamond markers), where the event reported in Chen et al. (2020) is labeled as event LHDW1 (Δt = 05:27:07.15–05:27:07:75 on 2017-07-03) and the event reported in Cozzani et al. (2021) is labeled as LHDW2 (Δt = 12:18:30.30–12:18:36.50, $\Delta_{\mathcal{T}_{EFI}>0}$ = 12:18:32.07–12:18:33.54 on 2017-08-10). We note that while the EFI threshold is reached during event LHDW2, it is never reached for LHDW1, neither during the interval of wave activity nor considering an interval of several seconds centered around the interval of wave activity. For this reason, we could not define $\Delta_{\mathcal{T}_{EFI}>0}$ for event LHDW1. Both events present characteristics that are similar to the EF events ($k\rho_e \lesssim 1$, oblique θ_{kB} and $\mathcal{E}_{long} \lesssim 0.5$). However, for LHDW2 we observe a non-zero frequency (see Fig. 10(a) and (b)), so the observed waves could not be identified as non-propagating EF waves. Concerning event LHDW1, while the observed frequency (black diamond in Fig. 10(a) and (b)) lies inside the variability range $\sigma_{f_{DS}}$, we note that $\sigma_{f_{DS}}$ is at least four times larger than any $\sigma_{f_{DS}}$ computed for the EF events, indicating that the measurement is not reliable in this case. Also, the behavior of f_{DS} is drastically different in LHDW1 and the EF events. During the EF events, we observe the Doppler shift frequency f_{DS} fluctuating around the value of the observed frequency f_{obs} so that for several points in the time interval with wave activity $f_{DS} = f_{obs}$ (see e.g. Fig.7(c)). In contrast, during the wave activity interval of event LHDW1, f_{DS} does not fluctuate around f_{obs} (not shown); it varies approximately linearly during the considered interval and it takes the value f_{obs} only twice. More importantly, the EFI instability threshold is never exceeded during event LHDW1. Hence, it is unlikely that EFI-generated waves would be observed during event LHDW1. We conclude that, while the observed EF and LHDW waves share some similarities, it is possible to distinguish between the two modes. This comparison further confirms that the reported events are reliably identified as EF fluctuations.

As mentioned in previous sections, during several of the EF events, the waves that we have identified as EFI-generated are not observed in correspondence of the EF unstable intervals where $\mathcal{T}_{EFI} > 0$, but rather immediately before or after. This may be unexpected as we might expect to observe the EF waves in the source region, as they are non-propagating fluctuations. At the same time, we expect the electron temperature anisotropy to decrease as the waves grow and the instability proceeds to the non-linear stage leading to electron isotropization. This means that MMS could observe a region with unstable plasma without (prior to) wave development and observe clear wave activity in a region where the instability has already saturated and reduced the anisotropy of the plasma, so it is stable to EFI at the time of the observations.

The validity of this interpretation depends on the time scales associated with the development and saturation of EFI compared to the duration of the observed intervals with $\mathcal{T}_{EFI} > 0$ and of the intervals with wave activity. The time scales of interest are

related to the wave growth rate γ, $T_\gamma = 2\pi/\gamma$ and to the time required to reach the maximum fluctuations amplitude T_{peak}. These two quantities cannot be easily computed with in situ measurements. However, we can obtain an estimation of T_γ from the results of the linear solver. The time scale T_{peak} has been evaluated in simulation studies. The value of T_{peak} is quite similar in simulation studies by Gary and Nishimura (2003); Camporeale and Burgess (2008); Hellinger et al. (2014) and corresponds to $T_{peak} \approx 5{-}10\ T_{\gamma_{max}}$, where $T_{\gamma_{max}} = 2\pi/\gamma_{max}$ is computed for the maximum growth rate. In the case of event #6, the interval where the EFI threshold is exceeded, $\Delta t_{\mathcal{T}_{EFI}>0}$, has a duration of 0.49 s. The maximum growth rate is $\gamma_{max} = 0.025\ \Omega_{ce}$ (see Fig.8(a)) so that $T_{\gamma_{max}} = 2\pi/\gamma_{max} =$ 0.43 s (here $\Omega_{ce} = 580$ rad/s for a background magnetic field of 3 nT). Considering the estimate value of T_{peak} based on simulations results, $T_{peak} \approx 5 - 10T_{\gamma_{max}} \approx 2.15 -$ 4.3 s. Hence, $T_{peak} = 4.4{-}8.7\ \Delta t_{\mathcal{T}_{EFI}>0}$, meaning that the time spent by MMS in the unstable region is not enough to observe the wave development. At the same time, it is not surprising that the waves remain in the region where the temperature anisotropy is already being reduced, as the waves are non-propagating. This estimation yields to similar results also for the other events that have the wave activity not co-located with $\Delta t_{\mathcal{T}_{EFI}>0}$. This simple qualitative estimation, despite its inherent limitations, can help us understand the lack of wave observations in the intervals with $\mathcal{T}_{EFI} > 0$.

The observed EF fluctuations are located in the reconnection outflow, which is characterized by strong flow. It is worth underlining that the presence of this strong electron flow is crucial for observing the non-propagating EF mode as it allows for a significant Doppler shift frequency that, in the case of non-propagating modes, will coincide with the observed frequency ($f_{obs} = f_{DS} \pm \sigma_{f_{DS}}$). We note, however, that a non-negligible Doppler shift frequency depends not only upon the magnitude of $\mathbf{v}_e$ but also on the angle between $\mathbf{v}_e$ and $\mathbf{k}$. In all considered events, $\mathbf{v}_e$ has a significant component along the wave vector yielding significant Doppler shift frequency.

Interestingly, for all the EF events the observed waves are more complex than predicted by linear dispersion theory. The observed EF waves exhibit magnetic field fluctuations of similar amplitude for all three components in both GSM and field-aligned (FAC) coordinate systems (see Fig.4(b) and Fig.5(b) for event #6; Fig.6(b) and Fig.7(b) for event #7). This is in contrast with the linear theory predicting low $\delta B_{||}/\delta B$, meaning that the components perpendicular to the background magnetic field are dominating the fluctuations (see Fig.1(d) and Fig.8(c), 9(c)). Also, while all the observed waves have a clear electromagnetic component, for several events $\langle \mathcal{E}_{long} \rangle_{\Delta t, \Delta f} \sim 0.5$ further indicating that the observed waves are quite complex as they are not fully electromagnetic or electrostatic.

9 Conclusions

We used high-resolution in situ measurements by MMS to investigate EFI-generated fluctuations in the outflow region of magnetic reconnection. We considered a current sheet flapping event in the Earth's magnetotail when MMS was almost continuously measuring the reconnection exhaust (both tailward and Earthward flow). We identified seven events characterized by wave activity during which the EFI threshold is exceeded.

Our results show that the observed waves have properties consistent with the non-propagating EF mode as predicted by the linear kinetic dispersion theory. In particular, we observe non-propagating fluctuations (i.e. zero real frequency) characterized by a wave vector $k\rho_e \lesssim 1$ directed obliquely with respect to the background magnetic field, with significant electromagnetic component and resonant with electrons. However, there are also some differences between the observed fluctuations and the prediction of the linear theory. Notably, all three fluctuating magnetic field components have similar amplitude; the waves are not fully electromagnetic or electrostatic, i.e. $\langle \mathcal{E}_{long} \rangle_{\Delta t, \Delta f} \sim 0.5$.

The investigation of the EF modes in the reconnection outflow region is crucial to improve our knowledge of the global energy conversion associated with reconnection. Indeed, the EFI-generated fluctuations are likely to lead to particle scattering and enhanced wave-particle interaction which in turn can affect particle energization and energy conversion during reconnection, ultimately altering the global energy budget of the magnetic reconnection process. This study, reporting for the first time direct observations of the EFI-generated fluctuations, represents the first step toward a more complete understanding of the EFI and its possible interplay with reconnection.

The results of this work are also beneficial to the study of the EFI in other plasma environments and regimes. In particular, the EFI is thought to play a key role in electron distribution isotropization in the solar wind but direct observation of the EF mode is currently prevented by the limited time resolution of particle measurements and lack of multi-spacecraft observations.

Open Research: Data Availability Statement

MMS data are available at `https://lasp.colorado.edu/mms/sdc/public/data/` following the directories: mms#/fgm/brst/l2 for FGM data, mms#/edp/brst/l2 for EDP data, mms#/fpi/brst/l2/dis-dist for FPI ion distributions, mms#/fpi/brst/l2/dis-moms for FPI ion moments, mms#/fpi/brst/l2/des-dist for FPI electron distributions, and mms#/fpi/brst/l2/des-moms for FPI electron moments. Data analysis was performed using the IRFU-Matlab analysis package, available at `https://github.com/irfu/irfu-matlab`. The PDRK numerical solver code is available at `https://github.com/hsxie/pdrk`.

Acknowledgments
The authors thank the entire MMS team and instruments' principal investigators for data access and support. Thank you to Konrad Steinvall for helpful discussions. GC is supported by the European Research Council Consolidator grant 682068-PRESTISSIMO. DBG is supported by the Swedish National Space Agency (SNSA), grant 128/17.

References

Biskamp, D. (2000). *Magnetic reconnection in plasmas*. Cambridge University Press. doi: 10.1017/CBO9780511599958

Burch, J., Moore, T., Torbert, R., & Giles, B. (2016, 05). Magnetospheric multiscale overview and science objectives. *Space Science Reviews*, *199*, 5-21. doi: 10.1007/s11214-015-0164-9

Camporeale, E., & Burgess, D. (2008). Electron firehose instability: Kinetic linear theory and two-dimensional particle-in-cell simulations. *Journal of Geophysical Research: Space Physics*, *113*(A7). doi: https://doi.org/10.1029/2008JA013043

Cattell, C., Breneman, A., Dombeck, J., Hanson, E., Johnson, M., Halekas, J., ... Whittlesey, P. (2022, jan). Parker solar probe evidence for the absence of whistlers close to the sun to scatter strahl and to regulate heat flux. *The Astrophysical Journal Letters*, *924*(2), L33. doi: 10.3847/2041-8213/ac4015

Chen, L.-J., Wang, S., Le Contel, O., Rager, A., Hesse, M., Drake, J., ... Avanov, L. (2020, Jul). Lower-hybrid drift waves driving electron nongyrotropic heating and vortical flows in a magnetic reconnection layer. *Phys. Rev. Lett.*, *125*, 025103. doi: 10.1103/PhysRevLett.125.025103

Chew, G. F., Goldberger, M. L., Low, F. E., & Chandrasekhar, S. (1956). The boltzmann equation an d the one-fluid hydromagnetic equations in the absence of particle collisions. *Proceedings of the Royal Society of London. Series A. Mathematical and Physical Sciences*, *236*(1204), 112-118. doi:

764 10.1098/rspa.1956.0116
765 Cozzani, G., Khotyaintsev, Y. V., Graham, D. B., Egedal, J., André, M., Vaivads,
766 A., ... Burch, J. L. (2021, Nov). Structure of a perturbed magnetic reconnec-
767 tion electron diffusion region in the earth's magnetotail. *Phys. Rev. Lett.*, *127*,
768 215101. doi: 10.1103/PhysRevLett.127.215101
769 Daughton, W. (2003). Electromagnetic properties of the lower-hybrid drift insta-
770 bility in a thin current sheet. *Physics of Plasmas*, *10*(8), 3103-3119. doi: 10
771 .1063/1.1594724
772 Egedal, J., Le, A., & Daughton, W. (2013). A review of pressure anisotropy caused
773 by electron trapping in collisionless plasma, and its implications for magnetic
774 reconnection. *Physics of Plasmas*, *20*(6), 061201. doi: 10.1063/1.4811092
775 Ergun, R. E., Tucker, S., Westfall, J., Goodrich, K. A., Malaspina, D. M., Sum-
776 mers, D., ... Cully, C. M. (2016). The axial double probe and fields signal
777 processing for the mms mission. *Space Science Reviews*, *199*, 167-188. doi:
778 10.1007/s11214-014-0115-x
779 Feldman, W. C., Asbridge, J. R., Bame, S. J., Montgomery, M. D., & Gary, S. P.
780 (1975). Solar wind electrons. *Journal of Geophysical Research (1896-1977)*,
781 *80*(31), 4181-4196. doi: https://doi.org/10.1029/JA080i031p04181
782 Gao, J. W., Rong, Z. J., Cai, Y. H., Lui, A. T. Y., Petrukovich, A. A., Shen, C.,
783 ... Wan, W. X. (2018). The distribution of two flapping types of mag-
784 netotail current sheet: Implication for the flapping mechanism. *Jour-*
785 *nal of Geophysical Research: Space Physics*, *123*(9), 7413-7423. doi:
786 https://doi.org/10.1029/2018JA025695
787 Gary, S. P. (1993). *Theory of space plasma microinstabilities*. Cambridge University
788 Press. doi: 10.1017/CBO9780511551512
789 Gary, S. P., Lavraud, B., Thomsen, M. F., Lefebvre, B., & Schwartz, S. J. (2005).
790 Electron anisotropy constraint in the magnetosheath: Cluster observa-
791 tions. *Geophysical Research Letters*, *32*(13). doi: https://doi.org/10.1029/
792 2005GL023234
793 Gary, S. P., & Madland, C. D. (1985). Electromagnetic electron temperature
794 anisotropy instabilities. *Journal of Geophysical Research: Space Physics*,
795 *90*(A8), 7607-7610. doi: https://doi.org/10.1029/JA090iA08p07607
796 Gary, S. P., & Nishimura, K. (2003). Resonant electron firehose instability: Particle-
797 in-cell simulations. *Physics of Plasmas*, *10*(9), 3571-3576. doi: 10.1063/1
798 .1590982
799 Gary, S. P., Smith, C. W., Lee, M. A., Goldstein, M. L., & Forslund, D. W. (1984).
800 Electromagnetic ion beam instabilities. *The Physics of Fluids*, *27*(7), 1852-
801 1862. doi: 10.1063/1.864797
802 Graham, D. B., Khotyaintsev, Y. V., Norgren, C., Vaivads, A., André, M., Drake,
803 J. F., ... Ergun, R. E. (2019). Universality of lower hybrid waves at earth's
804 magnetopause. *Journal of Geophysical Research: Space Physics*, *124*(11),
805 8727-8760. doi: https://doi.org/10.1029/2019JA027155
806 Graham, D. B., Khotyaintsev, Y. V., Vaivads, A., & André, M. (2016). Electro-
807 static solitary waves and electrostatic waves at the magnetopause. *Journal of*
808 *Geophysical Research: Space Physics*, *121*(4), 3069-3092. doi: https://doi.org/
809 10.1002/2015JA021527
810 Hellinger, P., Trávníček, P. M., Decyk, V. K., & Schriver, D. (2014). Oblique
811 electron fire hose instability: Particle-in-cell simulations. *Journal of Geophys-*
812 *ical Research: Space Physics*, *119*(1), 59-68. doi: https://doi.org/10.1002/
813 2013JA019227
814 Hollweg, J. V., & Völk, H. J. (1970). New plasma instabilities in the solar wind.
815 *Journal of Geophysical Research (1896-1977)*, *75*(28), 5297-5309. doi: https://
816 doi.org/10.1029/JA075i028p05297
817 Innocenti, M. E., Tenerani, A., Boella, E., & Velli, M. (2019, sep). Onset and
818 evolution of the oblique, resonant electron firehose instability in the ex-

panding solar wind plasma. *The Astrophysical Journal*, *883*(2), 146. doi: 10.3847/1538-4357/ab3e40

Lazar, M., Shaaban, S. M., Poedts, S., & Š. Štverák. (2016). Firehose constraints of the bi-kappa-distributed electrons: a zero-order approach for the suprathermal electrons in the solar wind. *Monthly Notices of the Royal Astronomical Society*, *464*(1), 564–571. doi: https://doi.org/10.1093/mnras/stw2336

Le, A., Stanier, A., Daughton, W., Ng, J., Egedal, J., Nystrom, W. D., & Bird, R. (2019). Three-dimensional stability of current sheets supported by electron pressure anisotropy. *Physics of Plasmas*, *26*(10), 102114. doi: 10.1063/1.5125014

Leonenko, M. V., Grigorenko, E. E., Zelenyi, L. M., Malova, H. V., Malykhin, A. Y., Popov, V. Y., & Büchner, J. (2021). Mms observations of super thin electron-scale current sheets in the earth's magnetotail. *Journal of Geophysical Research: Space Physics*, *126*(11), e2021JA029641. doi: https://doi.org/10.1029/2021JA029641

Li, X., & Habbal, S. R. (2000). Electron kinetic firehose instability. *Journal of Geophysical Research: Space Physics*, *105*(A12), 27377-27385. doi: https://doi.org/10.1029/2000JA000063

Lindqvist, P.-A., Olsson, G., Torbert, R., King, B., Granoff, M., Rau, D., ... Tucker, S. (2016). The spin-plane double probe electric field instrument for mms. *Space Science Reviews*, *199*, 137–165. doi: 10.1007/s11214-014-0116-9

López, R. A., Micera, A., Lazar, M., Poedts, S., Lapenta, G., Zhukov, A. N., ... Shaaban, S. M. (2022, may). Mixing the solar wind proton and electron scales. theory and 2d-PIC simulations of firehose instability. *The Astrophysical Journal*, *930*(2), 158. doi: 10.3847/1538-4357/ac66e4

Maneva, Y., Lazar, M., Viñas, A., & Poedts, S. (2016, nov). MIXING THE SOLAR WIND PROTON AND ELECTRON SCALES: EFFECTS OF ELECTRON TEMPERATURE ANISOTROPY ON THE OBLIQUE PROTON FIREHOSE INSTABILITY. *The Astrophysical Journal*, *832*(1), 64. doi: 10.3847/0004-637x/832/1/64

Messmer, P. (2002). Temperature isotropization in solar flare plasmas due to the electron firehose instability. *A&A*, *382*(1), 301-311. doi: 10.1051/0004-6361:20011583

Paesold, G., & Benz, A. O. (2003). Test particle simulation of the electron firehose instability. *A&A*, *401*(2), 711-720. doi: 10.1051/0004-6361:20030113

Pilipp, W., & Völk, H. J. (1971). Analysis of electromagnetic instabilities parallel to the magnetic field. *Journal of Plasma Physics*, *6*(1), 1–17. doi: 10.1017/S0022377800025654

Pilipp, W. G., Miggenrieder, H., Montgomery, M. D., Mühlhäuser, K. H., Rosenbauer, H., & Schwenn, R. (1987). Characteristics of electron velocity distribution functions in the solar wind derived from the helios plasma experiment. *Journal of Geophysical Research: Space Physics*, *92*(A2), 1075-1092. doi: https://doi.org/10.1029/JA092iA02p01075

Pollock, C. J., Moore, T. E., Jacques, A. D., Burch, J. L., Gliese, U., Saito, Y., ... Zeuch, M. A. (2016). Fast plasma investigation for magnetospheric multiscale. *Space Science Reviews*, *199*, 331-406. doi: 10.1007/s11214-016-0245-4

Richard, L., Khotyaintsev, Y. V., Graham, D. B., Sitnov, M. I., Le Contel, O., & Lindqvist, P.-A. (2021). Observations of short-period ion-scale current sheet flapping. *Journal of Geophysical Research: Space Physics*, *126*(8), e2021JA029152. doi: https://doi.org/10.1029/2021JA029152

Russell, C. T., Anderson, B. J., Baumjohann, W., Bromund, K. R., Dearborn, D., Fischer, D., ... Richter, I. (2016). The magnetospheric multiscale magnetometers. *Space Science Reviews*, *199*, 189-256. doi: 10.1007/s11214-014-0057-3

Shaaban, S. M., Lazar, M., López, R. A., Yoon, P. H., & Poedts, S. (2021). Advanced interpretation of waves and instabilities in space plasmas. In

M. Lazar & H. Fichtner (Eds.), *Kappa distributions: From observational evidences via controversial predictions to a consistent theory of nonequilibrium plasmas* (pp. 185–218). Cham: Springer International Publishing. doi: 10.1007/978-3-030-82623-9_10

Shaaban, S. M., Lazar, M., López, R. A., Fichtner, H., & Poedts, S. (2019, mar). Firehose instabilities triggered by the solar wind suprathermal electrons. *Monthly Notices of the Royal Astronomical Society*, *483*(4), 5642–5648. doi: 10.1093/mnras/sty3377

Verscharen, D., Chandran, B. D. G., Boella, E., Halekas, J., Innocenti, M. E., Jagarlamudi, V. K., ... Whittlesey, P. L. (2022). Electron-driven instabilities in the solar wind. *Frontiers in Astronomy and Space Sciences*, *9*. doi: 10.3389/fspas.2022.951628

Štverák, v., Trávníček, P., Maksimovic, M., Marsch, E., Fazakerley, A. N., & Scime, E. E. (2008). Electron temperature anisotropy constraints in the solar wind. *Journal of Geophysical Research: Space Physics*, *113*(A3). doi: https://doi.org/10.1029/2007JA012733

Wang, S., Chen, L.-J., Bessho, N., Ng, J., Hesse, M., Graham, D. B., ... Giles, B. (2022). Lower-hybrid wave structures and interactions with electrons observed in magnetotail reconnection diffusion regions. *Journal of Geophysical Research: Space Physics*, *127*(5), e2021JA030109. (e2021JA030109 2021JA030109) doi: https://doi.org/10.1029/2021JA030109

Xie, H., & Xiao, Y. (2016). PDRK: A general kinetic dispersion relation solver for magnetized plasma. *Plasma Science and Technology*, *18*(2), 97–107. doi: 10.1088/1009-0630/18/2/01

Yoo, J., Ji, J.-Y., Ambat, M. V., Wang, S., Ji, H., Lo, J., ... Goodman, A. (2020). Lower hybrid drift waves during guide field reconnection. *Geophysical Research Letters*, *47*(21), e2020GL087192. doi: https://doi.org/10.1029/2020GL087192

Yoon, P. H., Lui, A. T. Y., & Sitnov, M. I. (2002). Generalized lower-hybrid drift instabilities in current-sheet equilibrium. *Physics of Plasmas*, *9*(5), 1526-1538. doi: 10.1063/1.1466822

Zhang, X., Angelopoulos, V., Artemyev, A. V., & Liu, J. (2018). Whistler and electron firehose instability control of electron distributions in and around dipolarizing flux bundles. *Geophysical Research Letters*, *45*(18), 9380-9389. doi: https://doi.org/10.1029/2018GL079613